Reverse engineering nuclear properties from rare earth abundances in the r process

M R Mumpower[1], G C McLaughlin[2], R Surman[3] and A W Steiner[4,5]

[1] Theoretical Division, Los Alamos National Lab, Los Alamos, NM 87545, USA
[2] Department of Physics, North Carolina State University, Raleigh, NC 27695, USA
[3] Department of Physics, University of Notre Dame, Notre Dame, IN 46556 USA
[4] Department of Physics and Astronomy, University of Tennessee, Knoxville, TN 37996, USA
[5] Physics Division, Oak Ridge National Laboratory, Oak Ridge, TN 37831, USA

E-mail: matthew@mumpower.net

Abstract

The bulk of the rare earth elements are believed to be synthesized in the rapid neutron capture process or r process of nucleosynthesis. The solar r-process residuals show a small peak in the rare earths around $A \sim 160$, which is proposed to be formed dynamically during the end phase of the r process by a pileup of material. This abundance feature is of particular importance as it is sensitive to both the nuclear physics inputs and the astrophysical conditions of the main r process. We explore the formation of the rare earth peak from the perspective of an inverse problem, using Monte Carlo studies of nuclear masses to investigate the unknown nuclear properties required to best match rare earth abundance sector of the solar isotopic residuals. When nuclear masses are changed, we recalculate the relevant β-decay properties and neutron capture rates in the rare earth region. The feedback provided by this observational constraint allows for the reverse engineering of nuclear properties far from stability where no experimental information exists. We investigate a range of astrophysical conditions with this method and show how these lead to different predictions in the nuclear properties influential to the formation of the rare earth peak. We conclude that targeted experimental campaigns in this region will help to resolve the type of conditions responsible for the production of the rare earth nuclei, and will provide new insights into the longstanding problem of the astrophysical site(s) of the r process.

(Some figures may appear in colour only in the online journal)

1. Introduction

One of the most intriguing open problems in nuclear astrophysics is the astrophysical site or sites of the production of the heaviest elements in the rapid neutron capture process, or r process, of nucleosynthesis [1, 2]. The final elemental and isotopic abundances of the nuclei produced in the r process can be seen in stars and found in meteorites [3]. From these observations one tries to determine the astrophysical conditions under which the r process occurs. Complicating this endeavor is a dearth of measurements of the properties of nuclei that participate in the r process. The study of the r process is therefore inherently an inverse problem—the output is known and the input must be determined.

The output, the observed isotopic and elemental abundance patterns, e.g. [4], show a number of interesting features. There exists evidence of both a 'weak' component to the r process [5–9], which produces material up until the region of atomic mass number $A \sim 120$, and a 'main' component which produces the rest of the heavier elements, $A \gtrsim 120$ [10–12]. A distinguishing factor between these two components is the scatter found in the elemental patterns of the weak component [13–15], suggesting either variable conditions within a single type of astrophysical event or contributions from multiple sites. Here we focus on the main component, which is characterized by the robustly-produced heavier r-process peaks found at $A \sim 160$ and $A \sim 195$, and likely also $A \sim 130$ [16, 17].

One component of the input, the astrophysical conditions, must be such that there is a high neutron flux [18, 19]. However, the precise amount of neutron-richness has not been established and neither has the degree of heating, or the range of outflow timescale, temperature or density. This has lead to a number of suggestions for the main r process site, which include the traditional core collapse supernova and the merging of compact objects; see [20–22] and references therein. Proposed r process sites show marked differences in the evolution of the last stage of the r process when nuclei slow their capture of neutrons and begin to decay back to stability, a phase known as 'freeze-out'. Though many variations are possible, conditions during the final of the r process can be generally classified as 'hot' or 'cold'. A hot r process evolution goes through an extended equilibrium between neutron captures and its inverse reaction photodissociation, often written, $(n, \gamma) \rightleftarrows (\gamma, n)$. The freeze-out from equilibrium and the decay back to stability are triggered by an exhaustion of free neutrons. A cold r process [23] evolution has a short or non-existent $(n, \gamma) \rightleftarrows (\gamma, n)$ phase where equilibrium fails due to the drop in temperature, followed by competition between neutron captures and β-decays.

The other component of the input for the r process is the yet to be measured nuclear properties of unstable neutron-rich nuclei. Theoretical nuclear models used in r-process calculations are well constrained and are mostly in agreement where data exists, however, the model predictions diverge as one approaches the driplines [24–26]. Where there is disagreement between models, there is no experimental data and the majority of nuclei that have substantial impact on the final r-process abundances are in this category, see [27–29] for recent examples. The most important nuclear physics inputs for the r process are masses, β-decays and neutron capture rates near closed neutron shells and in the rare earth region [22].

To solve an inverse problem, it is helpful to have the output as well determined as possible. The solar isotopic r-process abundances are defined by a residual procedure from the well constrained s-process abundances [30]. In particular, the abundances of the rare earth elements, the peak at $A \sim 160$, are some of the most precisely known in the solar system and

in very metal-poor stars [31]. Further, the *r*-process rare earths are expected to be produced only in the main *r* process, i.e. they do not have a weak component [14]. Therefore, the rare earth elements and the associated peak is an ideal choice for exploration of an *r* process inversion technique [32].

Two distinct mechanisms have been previously proposed to explain rare earth peak formation. The first mechanism is dynamic formation of the peak during freeze-out [33, 34]. In this scenario, material becomes hung up in the rare earth region during the decay back to stability. This mechanism requires a nuclear physics feature in this region responsible for the hangup and is sensitive to the late-time evolution of astrophysical conditions. The second mechanism is the formation of the peak by the deposition of fission fragments [35]. This possibility requires both multiple fission cycles from higher to lower atomic mass number and precisely tuned fission fragment distributions [36]. While a less aesthetically pleasing solution, it is also possible that the rare earth peak is formed by a combination of the two mechanisms. Experimental campaigns to produce the appropriate neutron-rich heavy fissioning isotopes are not possible now or in the foreseeable future. It may, however, be possible to extract information about fission barriers and yields with future experiments at radioactive beam facilities e.g. at the Facility for Rare Isotope Beams (FRIB) [37], the Facility for Antiproton and Ion Research (FAIR) [38] or at the radioactive beam factory at RIKEN [39]. In contrast, measurements of relatively lighter nuclei that are populated during the decay back to stability are possible in some cases currently and for others in near future. Ergo, the most sensible path forward is to try to confirm or eliminate the purely dynamical mechanism.

In this manuscript, we take the observed rare earth abundance pattern and, for different types of astrophysical conditions, invert this abundance pattern to determine nuclear properties. We use common Bayesian inference techniques [40–42] to find the region of the *NZ*-plane which dictates the shape and location of rare earth abundance pattern. The feedback provided by the observed rare earth abundances allows us to *reverse engineer* the required trends in the nuclear masses that are responsible for the production of the rare earth peak. The larger strategy is to compare predictions of this type with future measurements, moving us closer toward an understanding of the astrophysical site of the main *r* process. In section 2 we introduce this methodology and discuss all of the assumptions that go into our calculations. The propagation of nuclear model input changes is also covered in detail. In section 3 we give the results of these calculations and report the most favorable mass surface trends for each type of astrophysical conditions. In section 4 we summarize.

2. Methodology

The dynamical mechanism of rare earth peak formation requires a feature in the nuclear properties of rare-earth nuclei far from stability that causes a pileup of material as the *r*-process path moves toward stability. Pile-ups also occur in the main peaks which are thought to stem from closed shell structure at neutron numbers, $N = 82$ and $N = 126$ extending far from stability. The rare earth peak is smaller than the main peaks and therefore *a priori* one does not know if it originates from a nuclear structure feature that has a sharp transition in *N*, but has a large extent in *Z*, similar to what might happen at subshell closure or a feature with a more gentle slope, but also more localized in the (*N*, *Z*) plane.

It was suggested in the first work on the dynamical mechanism [33] that the feature originates from a deformation maximum that leads to a 'kink' in the neutron separation energies in this region. This kink was not the sharp feature seen at the closed shells, but instead of the smaller, more gentle type. In [33] it was suggested that when this more
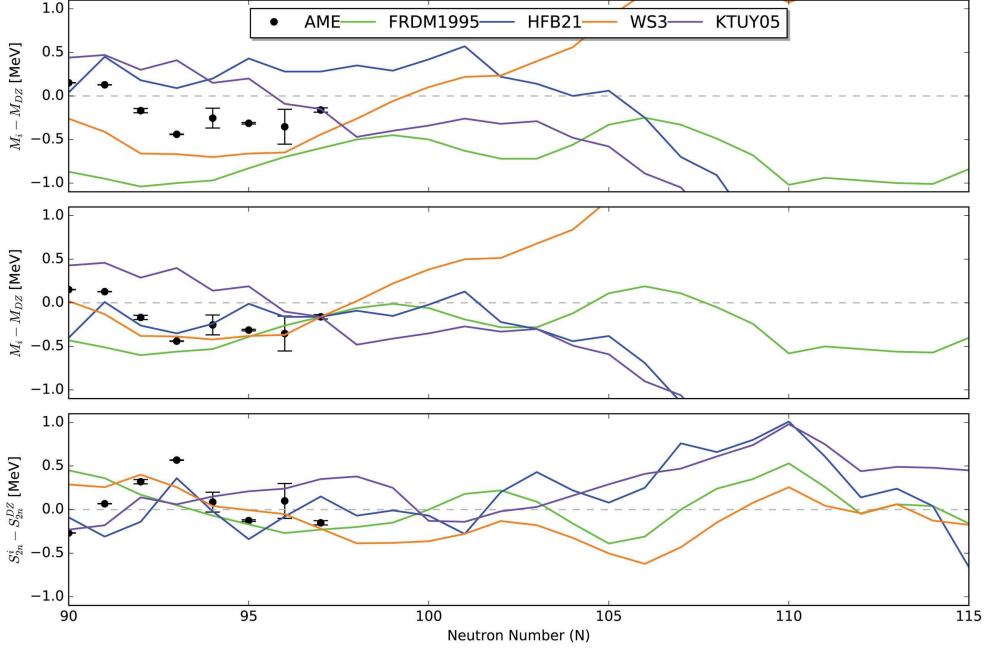
Figure 1. Mass predictions from several mass models [46–49] and measurements from the 2012 Atomic Mass Evaluation (AME2012) [50] are compared to the Duflo–Zuker [51] masses for the $Z = 60$ neodymium isotopic chain (top panel). Predicted trends in the mass surface are highlighted in the middle panel, which shows the same mass comparisons, scaled to the last mass measurement at $N = 97$. The bottom panel highlights trends in the mass surface using another measure, the difference in 2-neutron separation energies.

localized feature is encountered during the late stages of the r process, when $(n, \gamma) \rightleftarrows (\gamma, n)$ equilibrium is freezing out, material funnels into the kink region to create a peak. Later it was shown that a similar feature in neutron capture rates can create a peak in conditions where the bulk of the r process occurs out of equilibrium [34, 43]. While the structure of the mass surface is clearly essential to understanding the formation of the rare earth peak in the dynamical mechanism [44], the precise form of the structure has not yet been determined. The rare earth peak height and location are sensitive to both the astrophysical conditions at late times in the r process that govern the decay back to stability and the size and placement of the nuclear physics feature responsible for the pileup, which opens the possibility of constraining astrophysical conditions from the nuclear physics of the rare earth peak [45].

In this section we describe our methodology for treating the formation of the rare earths as an inverse problem. We utilize the sets of astrophysical conditions described in 2.6 and in the context of our model uncover the feature in the nuclear masses in the rare earth region that best reproduces the final isotopic abundance pattern for each set of conditions. We assume that the rare earth peak forms via the dynamical mechanism during the freeze-out phase of the r process, and that the nuclear feature responsible exists in the mass surface. We further assume the nuclear feature can be described by a function of neutron number, N, and proton number, Z. We use the Metropolis algorithm to explore the parameter space of our functional form for the nuclear masses. At each step in the Monte Carlo, we propagate the change in
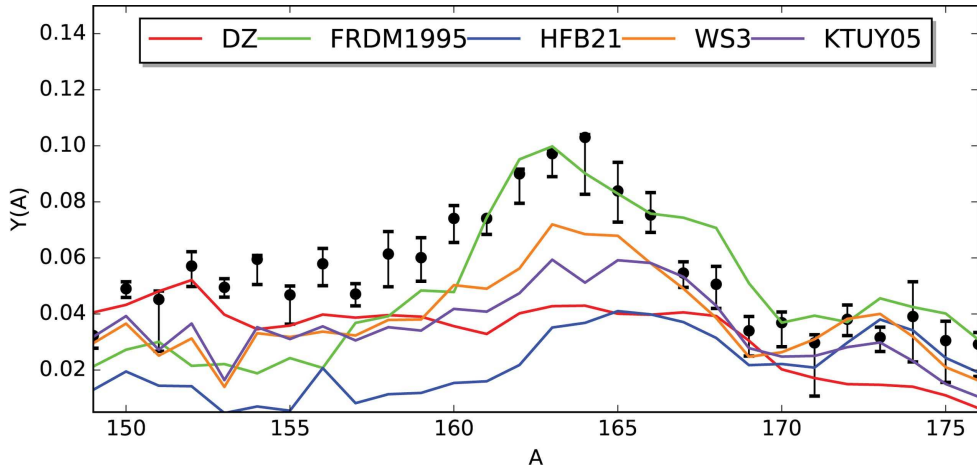
Figure 2. The final rare earth abundances from several mass models shown in figure 1 for hot *r*-process conditions—traj. 1 of this paper. The FRDM1995 and DZ lines represent consistently calculated datasets with all mass model changes propagated to the relevant quantities as outlined in section 2. For the remainder of the simulations, only the neutron separation energies change that go into the calculation of photodissociation rates. Unlike our reverse engineering framework, the β-decay rates from [52] and neutron capture rates [53] remain unchanged for HFB21, WS3 and KTUY05. Solar data from [20].

nuclear masses to other relevant quantities of the *r* process as in [26, 27]. The feedback, i.e. success or failure of a particular step in the Monte Carlo, is given by the match of the *r*-process network output to the observed rare earth abundances. We call this procedure the *reverse engineering* framework and now discuss the motivation for our approach followed by the details of the methodology.

2.1. Mass surface parameterization

We focus on nuclear masses between the $N = 82$ and $N = 126$ closed shells, since in previous work it was shown that the most crucial masses for the dynamical mechanism are centered near $N \sim 100$ [33, 34, 45]. The mass predictions of several mass models commonly used in *r*-process calculations are compared in figure 1 for the neodymium isotopic chain. Note the overall predictions of the mass models roughly agree to ± 0.5 MeV where data is available and diverge at higher neutron numbers. The nuclear data important for dynamical rare earth peak formation does not, however, depend on the absolute values of the masses but mass differences, e.g. neutron separation energies and *Q*-values. Therefore, the general trends in the mass surface are of greatest importance for the formation of the rare earth peak. These predicted trends, compared in the bottom panel of figure 1, show markedly different shapes and behaviors. When applied to *r*-process simulations, different mass models produce rare earth peaks with varying degrees of success [45], as shown in figure 2. Some theoretical nuclear mass models, such as the largely empirical Duflo–Zuker (DZ) [51] model, show no feature in this region, and thus *r*-process simulations run with these models do not exhibit dynamical rare earth peak formation, e.g. Figure 1 from [32]. Others, such as the 1995 version of the FRDM [46], find that the consequences of deformation are the prediction of a feature in the mass surface of sufficient depth to prompt rare earth peak formation, for certain ranges of
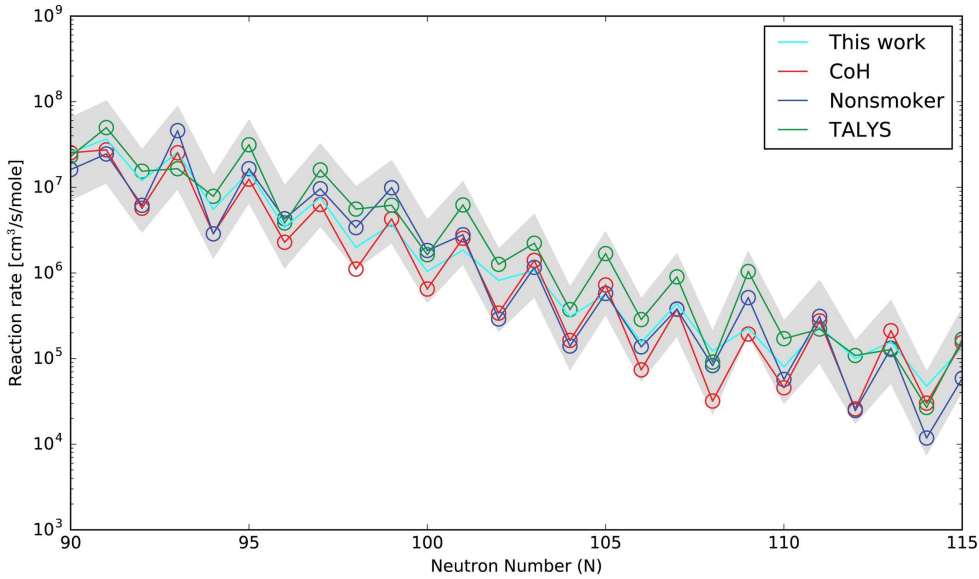
Figure 3. Theoretical astrophysical reaction rates along the $Z = 60$ neodymium isotopic chain for several statistical model codes [53, 57, 63] and the baseline values used in this work evaluated at a temperature $T = 1.0$ GK. Shaded band shows a factor of three variation from the average of the three statistical model predictions.

astrophysical conditions. For a discussion on how current uncertainties in mass models impact *r*-process abundances we point the reader to [22] and references therein.

If the rare earth peak forms via the dynamical mechanism, the structure in the mass surface that is responsible for peak formation may be localized in Z and N or exhibit a more global, smooth trend in the region. We would like to use an algorithm that allows for both possibilities. One possible starting point is to begin with a baseline mass model, and then produce small changes to each nuclear mass prediction in the rare earth region via Monte Carlo sampling until the peak has been produced. The problem with such an approach is the number of parameters quickly exceeds the number of observable rare earth abundances, as one parameter is needed per nucleus. This leads to an overdetermined system, which in all likelihood would converge to solutions that are not physically meaningful.

In our approach, we begin with the (DZ mass model [51], a model that exhibits no regional trend in the rare earth mass surface, and hence no rare earth peak. To account for the variety in possible mass surfaces (local or global) we modify the baseline DZ masses with an extra term,

$$M(Z, N) = M_{\mathrm{DZ}}(Z, N) + a_N e^{-(Z-C)^2/2f}, \tag{1}$$

where $M(Z, N)$ is the new mass prediction for the nucleus with Z protons and N neutrons, $M_{\mathrm{DZ}}(Z, N)$ is the baseline DZ mass, and the second term on the right hand side contains the mass modification parameters that will be run through the Monte Carlo procedure. Each isotone in the region, N ranging from 95 to 115, is assigned a unique coefficient, a_N. For a given neutron number, a_N controls the overall magnitude and sign of the mass change to the DZ model. The parameter C controls the center of the strength of the mass changes in proton number. If $Z = C$, the exponential term goes to unity and the mass changes from the a_N are maximal. We also incorporate a fall off parameter, f, which controls the rate at which the mass

modifications return return to zero, and the total mass prediction returns to the baseline DZ predictions in proton number. The fall off parameter ensures that any feature found in the mass surface responsible for peak formation disappears closer to stability, in accordance with measurements. The absence of an imposed functional form for the behavior of the mass surface as a function of neutron number, N, allows the algorithm to freely determine whether a kink structure exists or not. In principle there is the danger of converging on unphysical solutions with a_N allowed to flow freely, however, given the astrophysical conditions studied here, the solutions we find are always well behaved.

2.2. Neutron capture

The formation of the rare earth peak is also sensitive to the neutron capture rates in the region [44]. Neutron capture rates, which depend on the mass surface, in our reaction network are calculated using the Los Alamos statistical Hauser–Feshbach (HF) code, CoH (version 3.3.3) [54–57]. The most important model ingredients to this code besides the mass surface are the assumed level density (LD), the γ-strength function (γSF) and the particle optical model potential (OMP), see [58] for a discussion of popular codes and error analysis.

No neutron capture data exists for the neutron-rich nuclei that participate in the r process, thus the model ingredients all depend on theoretical calculations. CoH uses the Gilbert–Cameron LD [59] which is a hybrid description that uses a constant temperature model at low energies and matches to a Fermi gas model in the high energy regime that also includes shell corrections by Ignatyuk *et al* [60]. The γ-ray transmission coefficients are constructed using the generalized Lorentzian γSF [61] and the Koning–Delaroche global OMP is from [62]. Figure 3 shows the results of CoH calculations with DZ masses for the neodymium isotopic chain compared to neutron capture rate compilations commonly used in r-process simulations: NONSMOKER rates [53] with FRDM masses and TALYS [63] rates with HFB masses. While in some regions of the nuclear chart these rate compilations can disagree by orders of magnitude, in the rare earth region they agree within about a factor of 3 with similar model inputs.

The calculations of neutron capture rates are very time consuming, and so to good approximation one can capture the dependency of the change in masses by calculating the astrophysical reaction rate [33]

$$\lambda_{n,\gamma}(Z, N) = \exp[a(N, T) + b(N, T)S_n + c(N, T)S_n^2], \qquad (2)$$

where $a(N, T)$, $b(N, T)$ and $c(N, T)$ are temperature-dependent parameters for a given isotone, N, and S_n is the one neutron separation energy. The units of $\lambda_{n,\gamma}$ are taken to be $\mathrm{cm^3\,mole^{-1}\,s^{-1}}$. The rates are fit to the predictions of CoH using the baseline DZ masses on a temperature grid which fixes a, b and c for a given temperature T. These temperature-dependent parameters do not change throughout any of the Monte Carlo calculations. The average ratio between the output of CoH and our approximation is about a factor of 1.5 for the $Z = 60$ isotopic chain, compared to the factor of 3 that results from applying CoH with a variety of mass models. Using this approximation we find around a factor of 2 (or less) change in rate for $\Delta S_n = 500$ keV, which is in agreement with typical factors obtained when performing the entire neutron capture rate calculation over again using CoH [27] or TALYS [26]. The results of this approximation are compared to the various neutron capture rate compilations in figure 3 for the $Z = 60$ isotopic chain. As seen from figure 3 the formulation is a reasonably good approximation to neutron capture rates and their dependence on nuclear masses. We find a similar trend among odd-Z nuclei. Different models have different degrees of odd–even staggering and typically smoother abundance patterns are produced when less
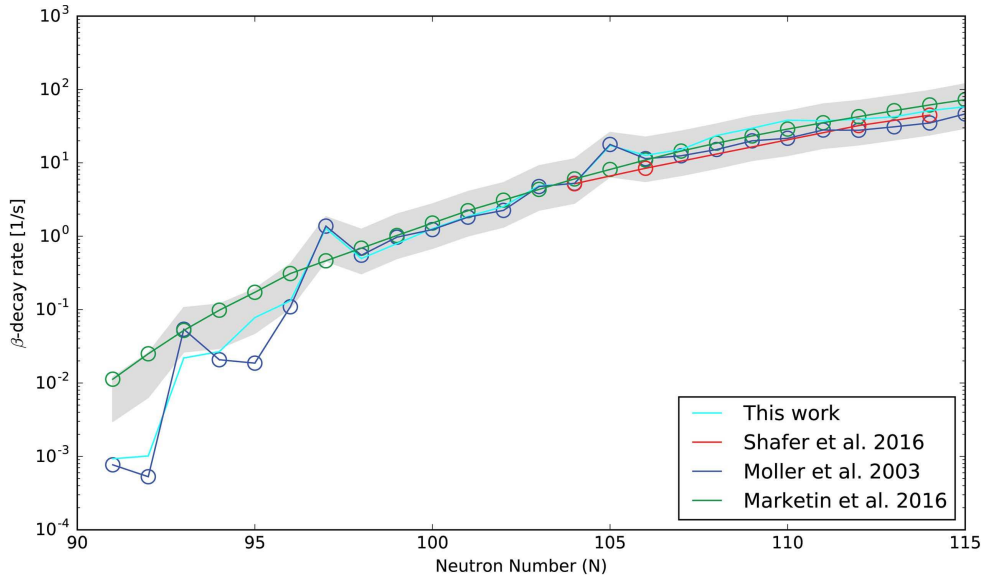
Figure 4. Theoretical β-decay rates for the $Z = 60$ neodymium isotopic chain from two compilations (Moller *et al* [52] and Marketin *et al* [67]) along with recent predictions from Shafer *et al* [65] and the baseline values predicted by this work.

odd–even staggering exists. Additional uncertainties in neutron capture rates that stem from the γSF are discussed in section 3.4.

2.3. β-decay

The β-decay properties of interest for *r*-process nucleosynthesis and rare earth peak formation are half-lives and delayed neutron emission probabilities [22, 33, 45, 64–66]. Both quantities depend on a theoretical description of the β-strength function, S_β, as well as the assumed mass surface of neutron-rich nuclei [52]. Close to stability, the energy window for β-decay, Q_β, is small, and the theoretical calculations are most sensitive to the details of the predicted nuclear structure. Further from stability, model predictions of β-decay rates are more consistent, with some variation coming from the assumed mass surface. In general, theoretical models of β-decay rates in the $N > 95$ region important for rare earth peak formation vary by only a factor of two or so, as shown for the neodymium isotopic chain in figure 4. Recently, it was shown that different Skyrme interactions in the finite-amplitude method [65] agree quite closely with the results of older quasi-particle random phase approximation (QRPA) calculations [52]. Variations of rates within the gray band of figure 4 may impact rare earth peak formation as shown in [65].

To study the variation in β-decay rates on the order of the size of the gray band in figure 4 we propagate the Monte Carlo mass surface changes from section 2.1 to the half-lives by recalculating:

$$T_{1/2}^{-1} = \sum_{0 \leqslant E_i \leqslant Q_\beta} S_\beta(E_i) \mathscr{F}(Z, R, Q_\beta - E_i), \tag{3}$$

where S_β is the β-strength function evaluated at excitation energy E_i in the daughter nucleus and $\mathscr{F}$ is the Fermi function evaluated with proton number Z, nuclear radius R and energy
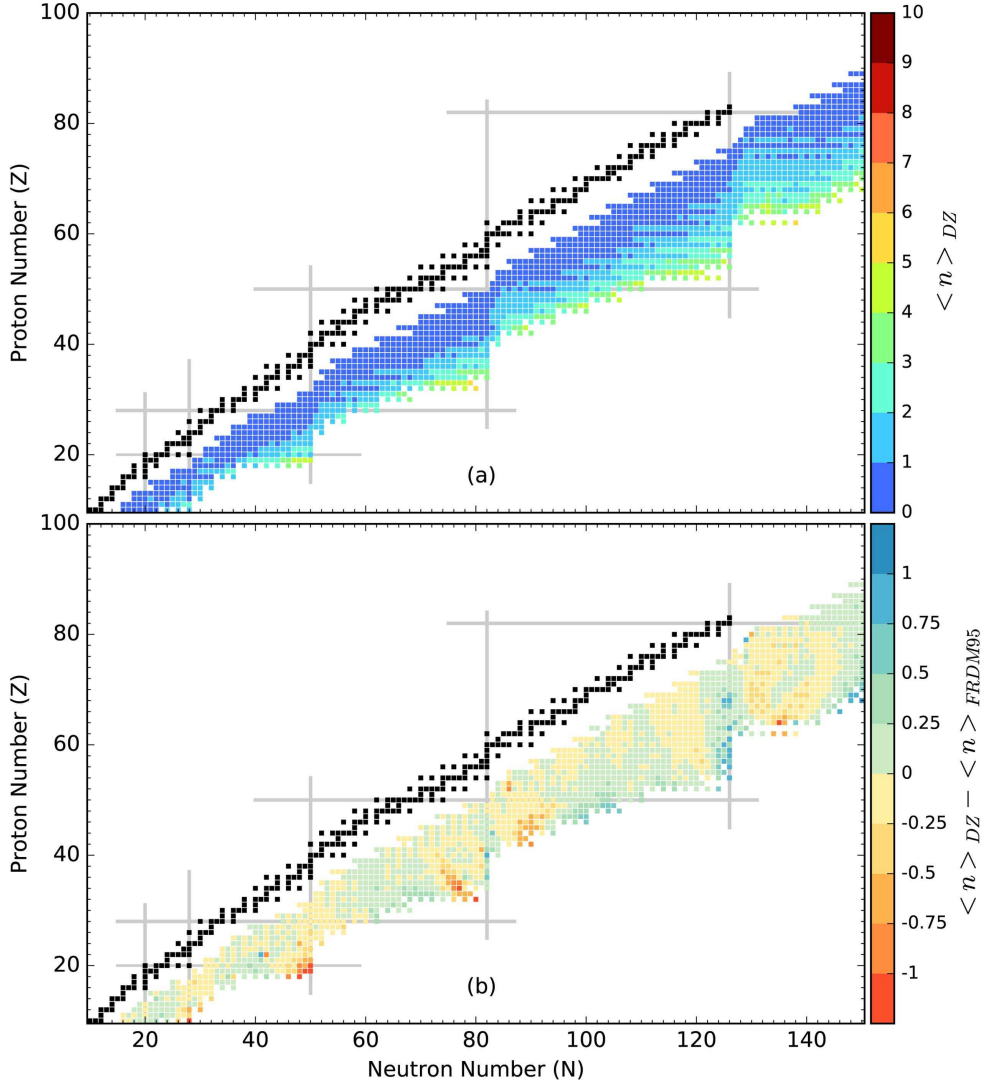
Figure 5. (a) Average number of neutrons emitted after β-decay using the QRPA+HF model assuming Duflo–Zuker masses. (b) Difference in neutrons emitted after β-decay using the QRPA+HF model for Duflo–Zuker and FRDM1995, which shows the impact of mass model assumptions on neutron emission after β-decay.

window $Q_\beta - E_i$. The summation runs over all the Gamow–Teller strength from the QRPA solutions of [68]. A change to nuclear masses can modify S_β, $\mathscr{F}$, and the limits of the summation in equation (3). The majority of the mass dependence sits in the phase space piece $\mathscr{F}$, which goes as the fifth power of the energy for allowed decays. The computationally-expensive nuclear matrix elements, in contrast, depend much less strongly on the masses. We therefore explore the impact of the change in Q_β on β-decay properties, which impacts both $\mathscr{F}$ and the summation limits, while leaving the β-strength function unchanged from [68]. This approximation has been used previously in [26, 27]. We find differences in Q_β of 500 keV yield roughly up to a factor of 2 or so change in the half-life.

We also propagate the mass changes to the prediction of β-delayed neutron emission probabilities, which we calculate by using the recently pioneered coupled QRPA+HF method [69]. In this method, neutron-gamma competition is tracked through subsequent generations during the statistical decay until all available excitation energy is spent. The probability to emit j-neutrons is given as a recursive convolution of level populations,

$$P_{jn}(E_{gs}) = \sum_{i=0}^{k-1} \mathscr{P}_j(E_i) p_j(E_i, E_{gs}) + \sum_{k'=0}^{k-1} \mathscr{P}_{j-1}(E_{k'}) q_{j-1}(E_{k'}, E_{gs}), \tag{4}$$

where $\mathscr{P}_j$ indicates the level population for the jth compound nucleus, p_j gives the probability to emit a γ-ray from an excited state to the ground state in the jth compound nucleus, q_{j-1} represents the probability to emit a neutron from the previous compound nucleus to the jth, the summations run over all levels which may feed the compound state k in jth compound nucleus, and the initial level population is given by the β-decay strength function, $\mathscr{P}_0(E_k) = S_\beta(E_k)$. For consistency, the same strength data as in the half-life calculation is used in the initial population of the compound daughter nucleus. Details of the QRPA+HF method and further discussion of equation (4), including the definition of the p and q functions, are given in [69].

Both Q_β and the neutron separation energies, S_n, are input arguments for the p and q functions, and a clear dependency of P_{jn} on these quantities is masked by the required convolution in equation (4). Thus it is important to propagate the mass changes all the way through in equation (4), as we do here. While, the intricate nature of the equation makes it difficult to gauge how mass changes will impact P_{jn} values, we do note that using DZ masses, a clear trend emerges with on average fewer neutrons emitted after β-decay than in the case of another popular mass model, FRDM1995. This can be seen by comparing the average number of neutrons emitted after β-decay, $\langle n \rangle$, in panel (a) of figure 5 to the results displayed in figure 6 of [69]. For convenience we provide this comparison in panel (b) of figure 5.

2.4. Fission

Because we seek a solution for rare earth peak formation that depends on the dynamical mechanism we employ a simple treatment of fission. We assume the dominant fission mechanism is the spontaneous fission of nuclei with $A > 250$, and we take the fission daughter product distributions to be a 57/43 split. This ensures that fission fragments fall in the $A \sim 130$ peak region and do not directly influence rare earth peak formation. In the splitting schema we employ here, we multiply the fissioning nucleus A and Z by 57, rounding to the nearest whole number to obtain the heavier fragment and subtract from the original A and Z to obtain the lighter fragment. The remainder (if any) goes to emitted neutrons to preserve the original mass number. Additionally, the daughter products are well away from the path on the neutron-rich side and emit multiple neutrons on the way back to the path. In our calculations, we find on average $6 - 9$ neutrons are emitted per fissioning nucleus in this manner. We also note that our framework can be expanded to models of fission that include the deposition of fission daughter products in the rare earth peak region. Fission inputs for r-process calculations remains an exciting and active area of research [70, 71].

2.5. Network calculations

The nuclear physics ingredients discussed above are coupled to astrophysical trajectories in a nuclear reaction network code. For our calculations we use the fast r-process network which is optimized to explore the freeze-out phase, most recently used in [22]. This network has
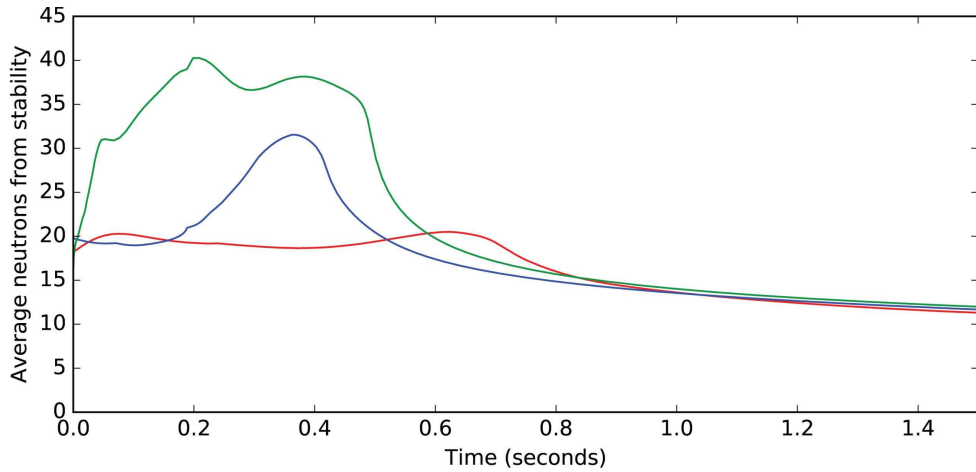
Figure 6. Average number of neutrons from stability for hot—traj. 1 (red), cold—traj. 4 (blue) and very neutron-rich cold—traj. 8 (green) astrophysical conditions during the freeze-out phase of the *r* process. Rare earth peak formation occurs when the nuclei begin to decay back to stability in each case. A time of zero indicates when the temperature has reached $T = 2.0$ GK.

channels for neutron capture, photodissociation, β-decay, β-delayed neutron emission, and fission and has robust support for modification of nuclear physics inputs. We start all of our nucleosynthesis calculations at $T = 2$ GK with realistic distributions of seed nuclei from a full charged-particle network [72]. The impact of charged-particle reactions during the formation of the rare earth peak is minimal as nearly all of these reactions have frozen out by the time the temperature reaches 2 GK, which is well before the formation of the rare earth peak in any of the considered scenarios. Alpha decays can play an important role for neutron-rich nuclei beyond the $N = 126$ shell closure and are thus crucial for the calculation of cosmo chronometers in the *r* process. However, they have little to no impact on the neutron-rich rare earth region so we do not include alpha decays in our network calculation. Further discussion of this *r*-process network can be found in [34, 44, 45].

2.6. Astrophysical conditions

Since the astrophysical site of the *r* process is uncertain, we select astrophysical trajectories that cover a broad spectrum of possibilities. To model a hot *r*-process which goes through an extended duration $(n, \gamma) \rightleftarrows (\gamma, n)$ equilibrium phase we select trajectories from parameterized winds entropies 30, 200, and 110 in units of k_B/baryon with timescales $\tau = 70, 80$, and 160 in units of ms and electron fractions $Y_e = 0.2, 0.3$, and 0.2, respectively [34]. We label these trajectories as trajectories 1, 2, and 3, respectively. For moderately cold *r*-process components with a short duration $(n, \gamma) \rightleftarrows (\gamma, n)$ equilibrium we choose a trajectory from a detailed supernova model with reheating [73], a wind parameterized as in [74] with entropy of 75 in units of k_B/baryon, $\tau = 75$ ms and $Y_e = 0.2$, and an extreme trajectory with very fast evolution, parameterized as in [45]: entropy of 125 in units of k_B/baryon, initial timescale of $\tau = 80$ ms, $Y_e = 0.2$, and freeze-out power law of $n = 6$. These are labeled trajectories 4, 5, and 6, respectively. For very neutron-rich cold *r*-process components we use trajectories, labeled 7, 8, and 9, from simulations of [75, 76]. A distinction between these three astrophysical evolutions is shown in figure 6. The very neutron-rich cold trajectories have an *r*-

Table 1. List of astrophysical trajectories used in this work. Values of quantities are quoted at a temperature of 10 GK. The units of entropy, s, are k_B/baryon, the units of dynamical timescale, τ, are in milliseconds and Y_e represents the electron fraction.

Traj.	Type	Description
1	Hot	Low entropy ($s = 30$) wind with $\tau = 70$ and $Y_e = 0.20$ [34]
2	Hot	High entropy ($s = 150$) wind with $\tau = 20$ and $Y_e = 0.30$ [34]
3	Hot	High entropy ($s = 200$) wind with $\tau = 80$ and $Y_e = 0.30$ [34]
4	Cold	Cold wind with reheating ($s = 70$) with $Y_e = 0.31$ [73]
5	Cold	Cold wind ($s = 75$) with $\tau = 75$ and $Y_e = 0.20$ [74]
6	Cold	Cold wind ($s = 125$) with $\tau = 80$, $n = 6.0$ and $Y_e = 0.20$ [45]
7	Very n-rich cold	Merger outflow ($s = 16$) with $Y_e = 0.019$ [75]
8	Very n-rich cold	Merger outflow ($s = 10$) with $Y_e = 0.050$ [76]
9	Very n-rich cold	Merger outflow ($s = 10$) with $Y_e = 0.016$ [75]

process path which ventures closer towards the neutron dripline relative to the hot and cold trajectories.

We summarize the choice of astrophysical trajectories in table 1. The high entropy conditions are possible in neutrino-driven wind environments, however we employ lower electron fractions than typically found in detailed supernova models [77] without exotic physics [78]. The low entropy conditions may be possible in an accretion disk wind with the expected values of Y_e. The very neutron-rich cold conditions used are possible in the tidal tail ejecta from neutron star-neutron star or neutron star-black hole mergers.

2.7. Algorithm

For each of our chosen astrophysical trajectories, we determine the mass surface that best reproduces the solar rare earth peak using our reverse engineering framework, based on the Metropolis algorithm [40]. Using Bayesian inference we can combine our prior distribution and our likelihood function to determine an updated posterior distribution. This approach is commonly used across the fields of physics and astronomy [41, 42]. In our case, we combine a Gaussian prior distribution in each of the nuclear masses to determine a new mass surface based off the evidence that we must reproduce the solar rare earth peak in addition to matching the the measured masses of the 2012 Atomic Mass Evaluation. We now outline how to use this technique in the context of our reverse engineering framework.

Our Monte Carlo parameters are defined by those appearing in the second term of equation (1): the a_N's, C, and sometimes f (if it is not held fixed). Each of these parameters is varied independently using Gaussian distributions with width 25 keV for the a_N's, 0.1 for C, and 0.5 for f. We start each Monte Carlo run by setting these parameters to zero, so that we begin with the baseline DZ prediction (no rare earth peak).

At the beginning of each Monte Carlo step we vary all the masses that enter into the reaction network by computing new parameter values and applying equation (1). For the DZ mass model this consists of roughly 500 nuclei that are in the range $A \sim 150$ to $A \sim 180$. Next, we propagate the changes produced by the small variations in the Monte Carlo parameters to the remainder of the r-process nuclear physics inputs as defined in sections 2.1–2.3.

The *r*-process network is then run with the nuclear physics ingredients from this particular set of Monte Carlo parameters.

The likelihood function for a given Monte Carlo step, *m*, is defined by

$$\mathcal{L}(m) = \exp\left[-\chi_r^2(m)/2 - \chi_m^2(m)/2\right], \tag{5}$$

where χ_r^2 represents the chi-squared function for matching the network abundance output to the solar isotopic pattern and χ_m^2 is the chi-squared function for matching the theoretical masses to the measured masses in the 2012 compilation [50].

More specifically, the chi-squared function for the *r* process for a given Monte Carlo step, *m*, is defined as

$$\chi_r^2(m) = \frac{1}{\Delta Y^2} \sum_{A=150}^{A=180} [Y_{\odot,r}(A) - Y(A))]^2, \tag{6}$$

where ΔY is the average observational uncertainty of the abundances in the rare earth region, $Y_{\odot,r}(A)$ is the isotopic solar *r*-process residual, $Y(A)$ is the isotopic sum of the output of our network calculation and the summation runs over *A*, the atomic mass number. The summation is limited in extent because we are only focused on the production of a local abundance feature, the rare earth peak. The lower limit in the solar isotopic residuals may not be defined, so for each *A* we take an approximate value of the observational uncertainty in the abundances of the rare earth region as $\Delta Y = 0.1$ dex.

We define a similar chi-squared function for the masses for a given Monte Carlo step, *m*,

$$\chi_m^2(m) = \frac{1}{\Delta M^2} \sum_{Z,N} [M_{\mathrm{AME}}(Z, N) - M(Z, N)]^2, \tag{7}$$

where $\Delta M = 405$ keV is taken to be the average root-mean-square value for DZ compared to the 2012 Atomic Mass Evaluation (AME2012), $M_{\mathrm{AME}}(Z, N)$ is the measured mass and $M(Z, N)$ is defined in equation (1) and the summation runs over all the nuclei with measured values in the AME2012.

To gauge the success or failure of a Monte Carlo step we compute the acceptance ratio,

$$\alpha(m) = \frac{\mathcal{L}(m)}{\mathcal{L}(m-1)}, \tag{8}$$

where $\mathcal{L}(m)$ is the likelihood function for the given step and $\mathcal{L}(m-1)$ is the likelihood function for the previous step. The baseline calculation using only DZ masses with all other parameters set to zero defines the likelihood function of the first step, $\mathcal{L}(0)$. If $\alpha(m) \geqslant 1$, the candidate step, *m*, is more likely than the previous, so we accept the step and update the parameters to the new values. If $\alpha(m) < 1$, the candidate step is taken with probability $\alpha(m)$, otherwise the step is rejected and the parameters are reset to those defined by the last successful step.

Because the predictions of measured masses remain relatively unchanged ($\chi_m^2 \sim 1.01$–1.03) due to our functional form from equation (1), we typically drop the second term of equation (5). In this case, the evolution of the Markov chain is only driven by the match of the network calculation to the solar abundances.

2.8. Convergence and error bars

The Monte Carlo procedure outlined in the previous subsection is repeated many times until the algorithm converges. At the end of each step in the Metropolis algorithm, the likelihood function is calculated to determined whether or not a step is successful. The running average
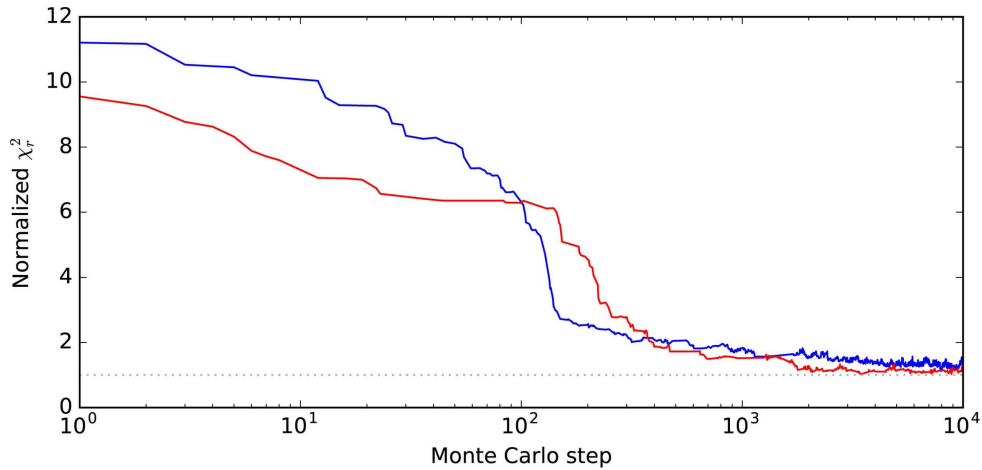
Figure 7. The evolution of the *r*-process chi-squared evaluated at successful Monte Carlo steps. The red curve indicates a run with the Monte Carlo parameters set to zero and the blue curve starts with Monte Carlo parameters varied randomly. Despite the difference in starting points, both runs eventually converge to the same solution after roughly 10 000 steps.
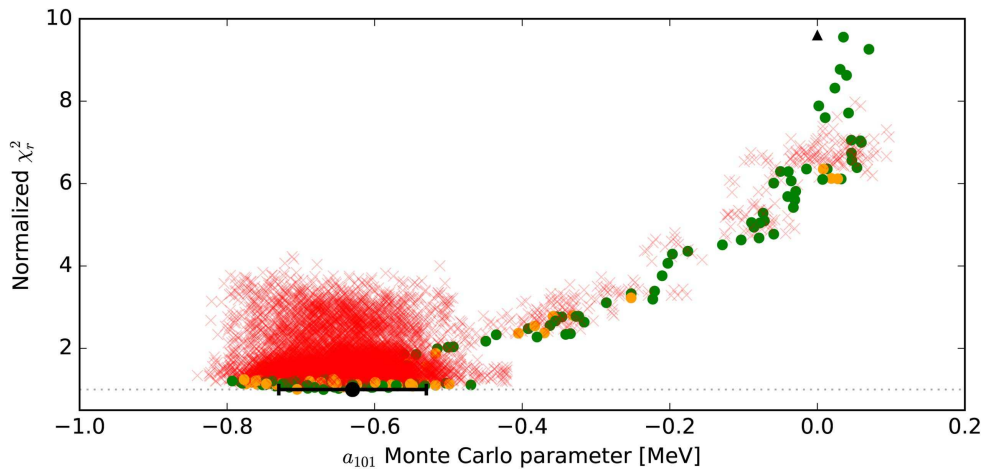

Figure 8. The progression of the *r*-process chi-squared as a function of the a_{101} Monte Carlo parameter in the case of a very neutron-rich cold *r*-process, traj. 8. The starting point (black triangle) is $a_{101} = 0$. Success steps are shown by filled green circles with failures denoted by red X's. Steps taken as successful with probability α from equation (8) are shown with yellow circles. A clear trend in this variable is observed with final prediction $a_{101} = -0.63 \pm 0.1\,\mathrm{MeV}$ denoted by the black circle and error bars.

of a parameter is then computed by averaging a list of current and past values. If the step is successful the current value of the parameter is appended to this list. Otherwise, the step is not successful and the value of the parameter from the most recent past successful step is used, which may fall back to the value of the parameter from the original step.
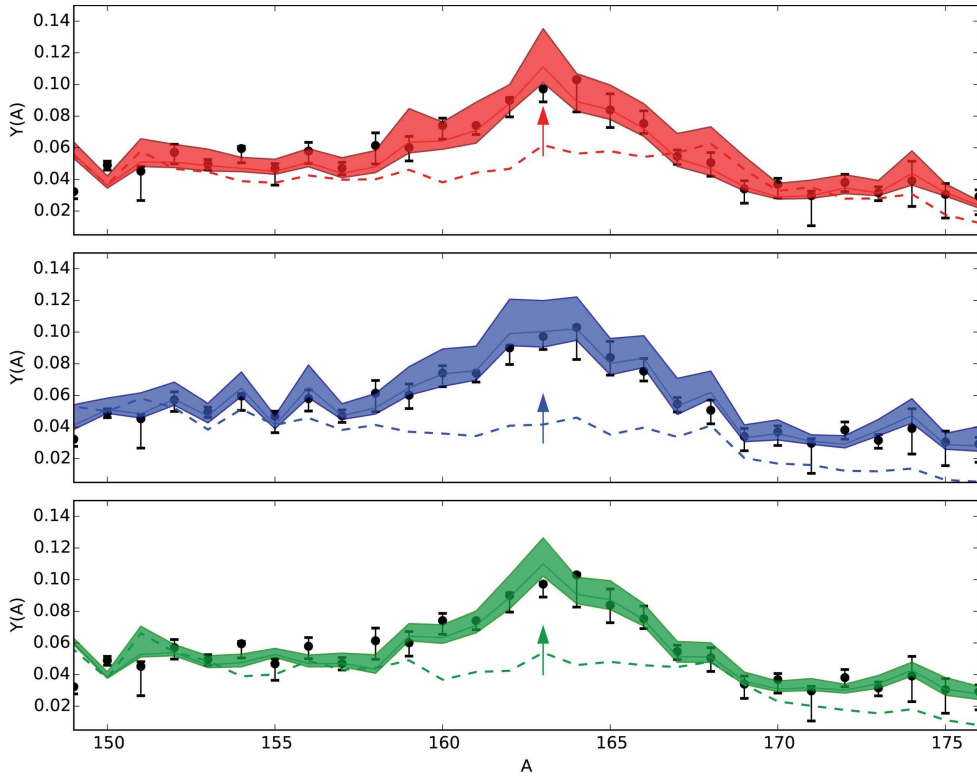
Figure 9. Final abundance predictions in the rare earth region on a linear scale for individual trajectories: hot—traj. 1 (top panel), cold—traj. 4 (middle panel) and very neutron-rich cold—traj. 8 (bottom panel) Metropolis runs. The application of the reverse engineering framework starts with the baseline (dashed curves) and produces the shaded region in each case.

We take the criterion for convergence to be that the running average of all of the parameters are within their respective standard deviations. This definition of convergence provides a necessary condition for reaching maximum likelihood since the running average of each parameter encodes the entire evolution of the Markov chain. When the algorithm is near maximum likelihood, the corresponding values of the parameters are averaged over with high occurrence, thus making them more important than the starting parameters. Parameters that have a large influence on the results will converge to some value but will have a very small variance, while those parameters with little impact will show a larger variation with mean of the original parameter value.

An example of the evolution of the *r*-process chi-squared, $\chi_r^2(m)$, for successful steps is shown in figure 7. It takes approximately 10 000 steps for the algorithm to find the solution starting with Monte Carlo parameters set to zero (red curve) or starting from a random set of values for Monte Carlo parameters (blue curve). Both of these curves converge to the same set of Monte Carlo parameters, which shows that our solutions are independent of starting position.

An example of the Markov chain evolution for a parameter in a very neutron-rich cold *r*-process is shown in figure 8. The black triangle represents the starting value of zero, while successful steps are shown by green dots. A yellow dot represents a step counted successful
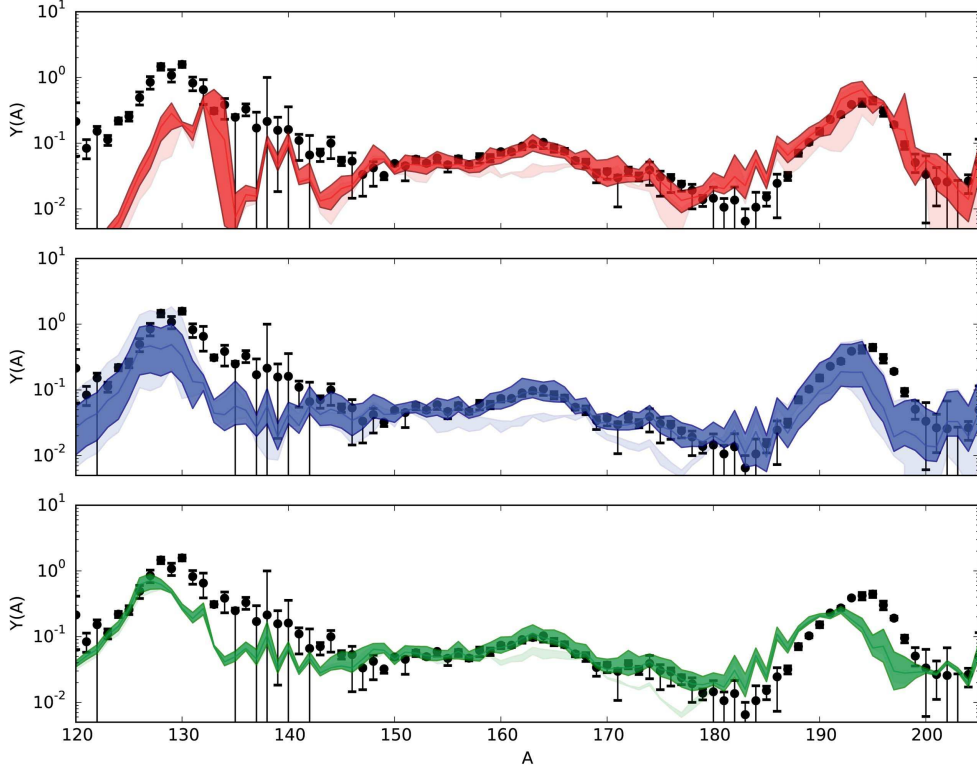
Figure 10. Dark shading shows final abundance predictions for the full range of the main *r* process on a log scale for trajectories combined by similar late-time evolutions: hot traj. 1–3 (top panel), cold traj. 4–6 (middle panel), and very neutron-rich cold traj. 7–9 (bottom panel). Light shading shows the range of the final abundances for the same combination of the baseline trajectories before the application of our framework.

with probability α from equation (8) and failure steps are denoted with a red X. This Markov chain produces a final prediction of $a_{101} = -0.63 \pm 0.1$ MeV denoted by black dot and error band. A small final error bar is seen in this Monte Carlo parameter which means it has a strong influence on the solution, as will be discussed in the results section.

3. Results

With the procedure outlined in section 2, we have defined a way of providing feedback to the nuclear physics by constraining our nuclear parameter space to be that which best matches the observed solar isotopic rare earth abundances. We are now ready to apply this framework to a number of astrophysical trajectories to reverse engineer the relevant nuclear properties important for the formation of the rare earth peak in each case.

3.1. Persistent rare earth feature

The trend in the mass surface that is responsible for the formation of the rare earth peak may be persistent, which means it spans a large range in proton number, or it may be more
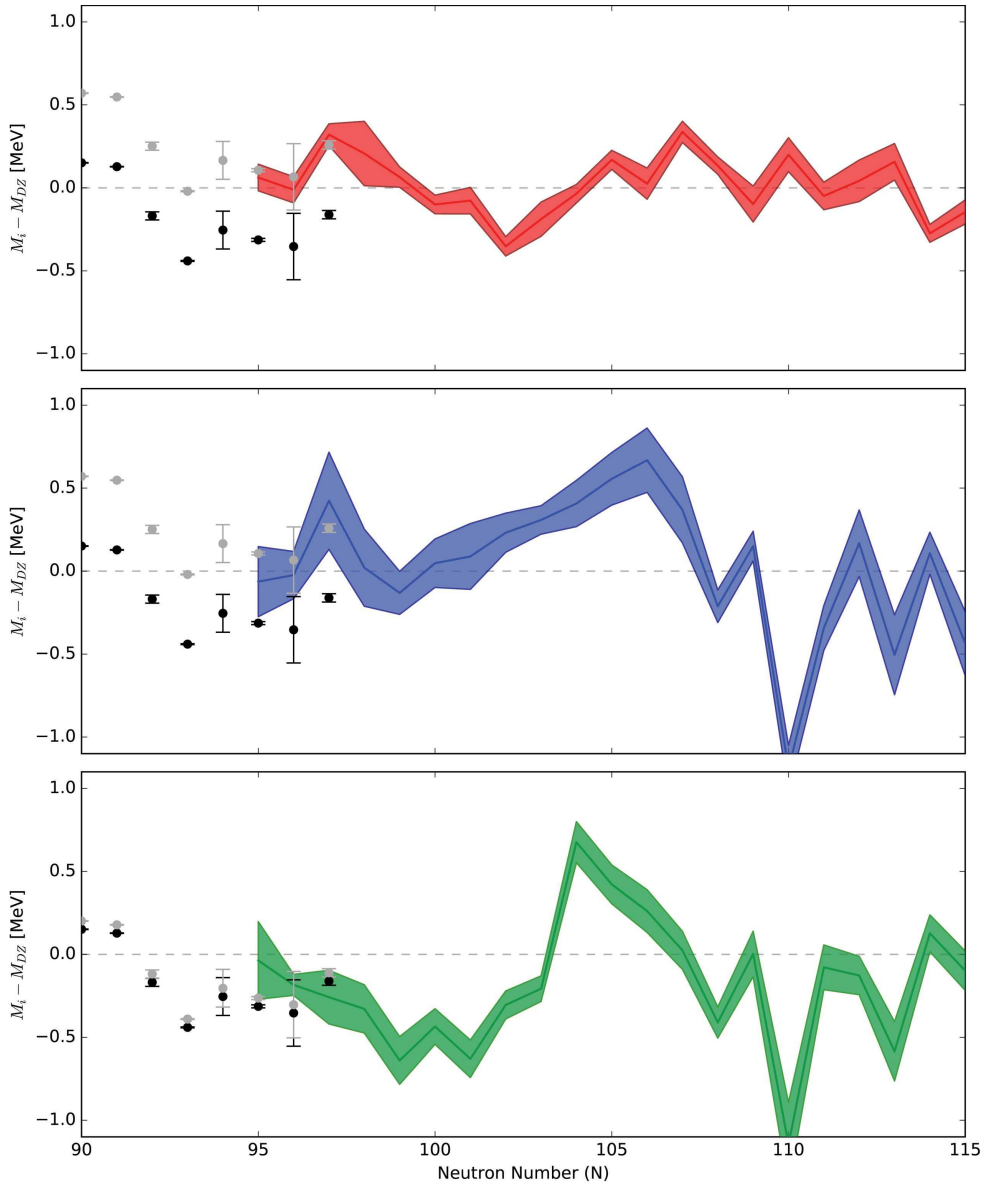
Figure 11. Predicted trends in the masses of $Z = 60$ neodymium isotopes for individual trajectories: hot—traj. 1 (top panel), cold—traj. 4 (middle panel) and very neutron-rich cold—traj. 8 (bottom panel) *r*-process conditions assuming a persistent feature ($f = 40$) in proton number after application of our reverse engineering framework. The 2012 AME masses are shown in black and shifted to match the mass surface prediction in gray.

localized in Z. We first discuss results assuming a persistent feature with $f = 40$ held fixed and the a_Ns and C allowed to vary.

The resultant final abundances with associated error bands are shown in figure 9 for individual astrophysical trajectories. The error bands represent the standard deviation of

previous steps as described in section 2.8. The simulations begin with unmodified DZ masses, which produce the abundance patterns given by the dotted curves. The application of our framework produces final abundance bands that are within the solar isotopic uncertainties for each A in the rare earth region. This shows the success of our algorithm and further indicates that our assumed abundance uncertainty of 0.1 dex for each isotopic abundance point is a very good approximation to the real uncertainties in the rare earth region.

The top panel of figure 9 shows a low entropy hot evolution (traj. 1), the middle panel shows a cold evolution (traj. 4) and the bottom panel shows a very neutron-rich cold evolution (traj. 8). The abundance patterns (including the baselines) are scaled to the $A \sim 150 - 180$ region for each set of conditions using the final simulation data from the Metropolis run. We find that in all cases the application of our framework successfully fills in the missing rare earth peak, and in the cold and very neutron-rich cold r-process conditions it also repairs the underproduction of material to the right of the peak.

Full abundance patterns for the main r process component are shown in figure 10. The top panel shows hot evolutions (traj. 1–3), the middle panel cold evolutions (traj. 4–6) and the bottom panel very neutron-rich cold evolutions (traj. 7–9). We find that the rare earth peak is well reproduced in all scenarios after application of our framework, indicated by the dark shading. The light shaded bands represent the range of the baseline final abundance patterns before the application of due to the variation in the similar astrophysical trajectories. We also note that rare earth masses have only a modest impact on the global pattern. This reinforces the conclusions of previous sensitivity studies, see e.g. [22].

We now seek to understand the trend in the mass surface responsible for the rare earth peak production. The predicted trends in the masses after application of our framework are shown in figure 11 for the same individual trajectories as in figure 9. Each mass surface shows a relative dip in the curve around $N \sim 100$. The dip represents a region that has locally enhanced stability, allowing material to be hung up when the r-process path passes through it. This is the feature which is responsible for the formation of the rare earth peak in the associated panels of figure 9.

We stress that it is the relative, overall trends in the masses that are important for rare earth peak formation, and not the absolute values of the masses. Thus in figure 11 we compare our resulting mass predictions to the AME2012 measurements in two ways: the black points show the raw values while the gray points are shifted to match the predicted curves from our algorithm. It is clear from the comparisons between our predictions and the shifted mass data that at this time one cannot rule out any of the possible mass surfaces without more measurements to constrain the trend in the region.

All trajectories require a dip to produce the rare earth peak, however, the trends of the mass surfaces are distinct in both the depth of the dip and its location depending on the astrophysical conditions. With the hot evolution, the dip is relatively shallow spanning no more than 0.8 MeV from highest to lowest point. In the very neutron-rich cold evolution, the dip is stronger, spanning over 1 MeV between highest and lowest points.

The position of the local minimums relative to the DZ masses also differs as shown in figure 11. For the hot evolution (top panel) the minimum is at $N = 102$. For both cold (middle panel) and very neutron-rich cold (bottom panel), the minimum is shifted to lower N, consistent with an initial formation of the peak at lower mass number, A. Cold evolutions tend to have a greater availability of neutrons at late times than hot scenarios, from fission and/or from the extra β-delayed neutron emission that comes from a path very far from stability. Thus we find the most favored solutions tend to initially populate a rare earth peak at lower A, and late-time neutron captures shift the peak to the correct placement. The position of the minimum may be around $N = 99$, or $N = 101$ in these two colder scenarios. The inclination
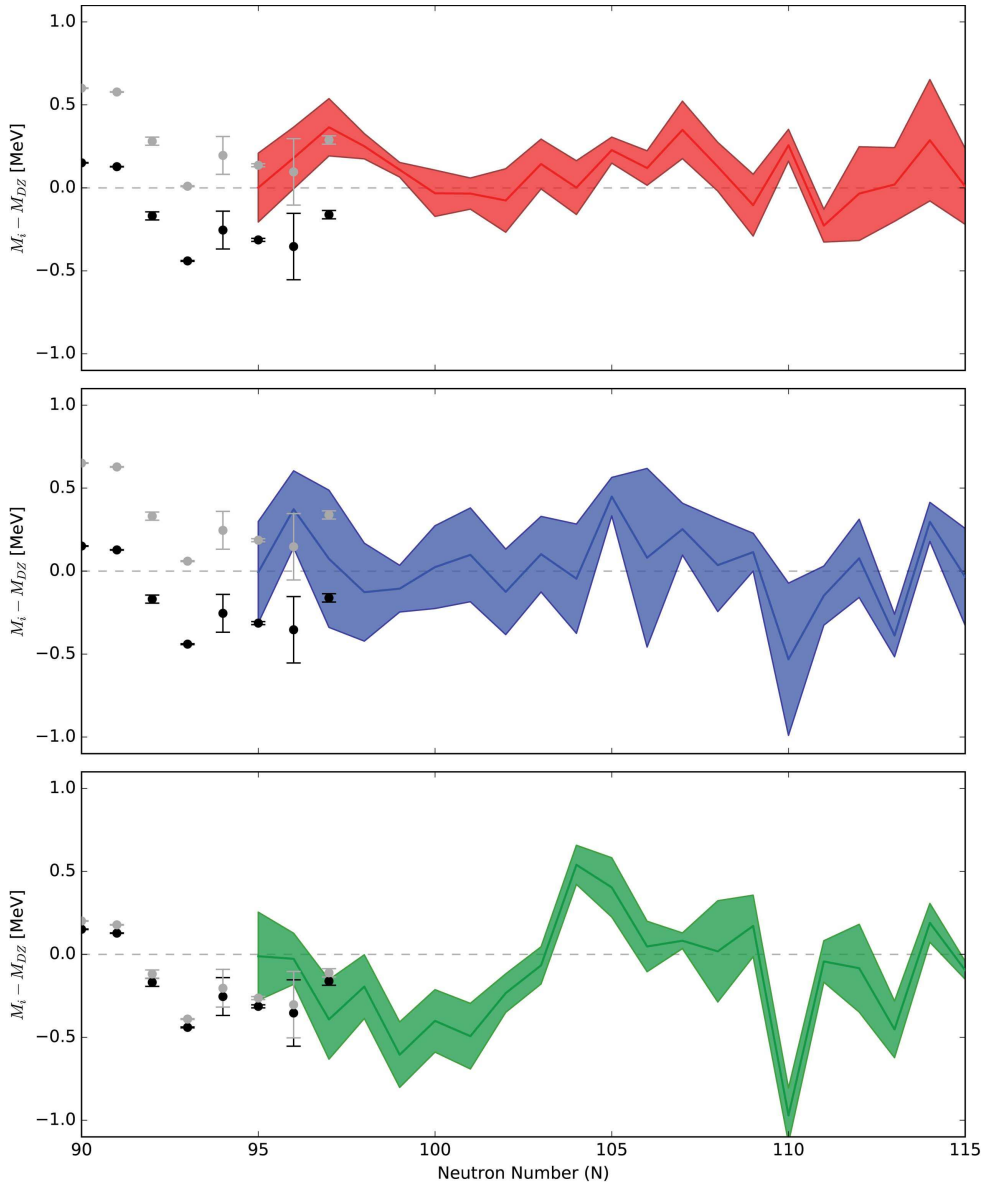
Figure 12. Combined mass surfaces for hot (top panel), cold (middle panel), and very neutron-rich cold (bottom panel) *r*-process conditions for the neodymium ($Z = 60$) isotopic chain assuming a persistent feature ($f = 40$) in proton number. The error band in these calculations represents a spreading of the parameter space which produces the rare earth peak due to the differences in evolution of similar astrophysical conditions.

to favor even-*N* in hot scenarios and odd-*N* in cold scenarios is connected to the rare earth peak formation mechanism. When $(n, \gamma) \rightleftarrows (\gamma, n)$ equilibrium persists for long times, such as in the hot conditions, a buildup of material occurs in even-*N* nuclei [33]. For colder scenarios, the path is entirely out of equilibrium and neutron capture rates are more important, thus favoring a dip at odd-*N* nuclei [34, 44].
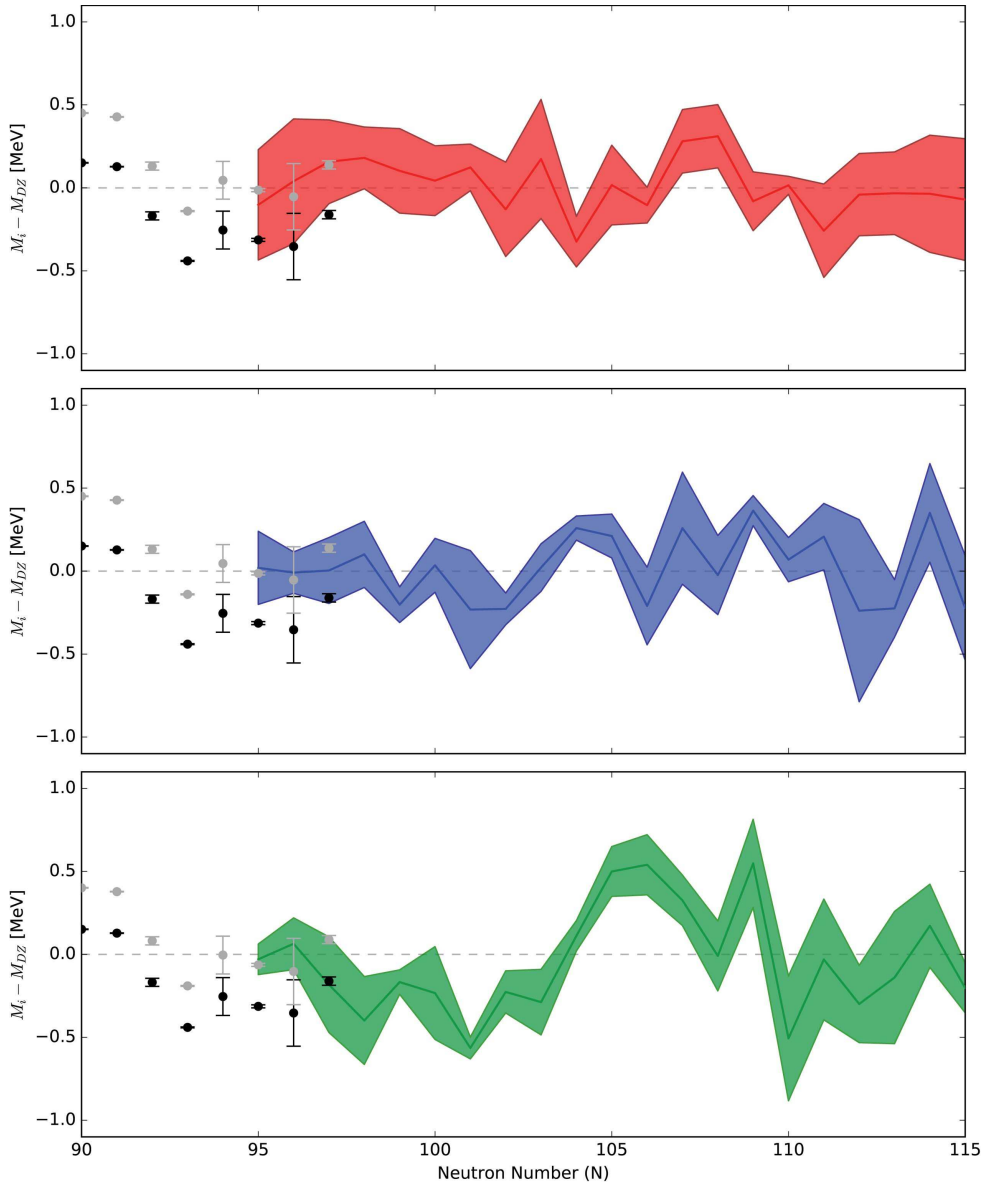
Figure 13. Combined mass surfaces for hot (top panel), cold (middle panel), and very neutron-rich cold (bottom panel) for the neodymium ($Z = 60$) isotopic chain assuming a localized feature ($f = 10$) in atomic number. The error bands again represent a spreading of the parameter space that produces the rare earth peak due to the differences in evolution of similar astrophysical conditions.

A second strong feature is noted near $N = 110$ in cold and very neutron-rich cold scenarios. We find this feature reduces the deficiencies seen to the right of the rare earth peak that exists in the baseline model, as observed in the bottom two panels of figure 9.

The position in the Z of maximal change in the masses from DZ is represented by the Monte Carlo parameter C in our parameterization. Assuming a persistent feature, each

trajectory studied shows C converge to $Z = 60$, or the neodymium isotopic chain. In our calculations, the final uncertainty for this parameter ranges from 0.1 to 0.6 in units of Z depending on the astrophysical conditions considered.

Figures 9 and 11 illustrate the success and power of our method. It would be of limited use, however, if we found distinct and dissimilar solutions for each individual astrophysical trajectory attempted. We find instead the exact opposite—similar mass surface trends are predicted for astrophysical trajectories within each late-time evolution characterization: hot (traj. 1–3), cold (traj. 4–6), and very neutron-rich cold (traj. 7–9).

Figure 12 shows the combined results of our Metropolis runs with hot trajectories 1–3, cold trajectories 4–6, and very neutron-rich cold trajectories 7–9. Again the predicted trends in the mass surfaces are shown along the $Z = 60$ (neodymium) isotopic chain. The error bands for the mass surface now represent a spreading of the parameter space from the combination of the three best fit solutions of similar late-time evolutions. Despite the spreading of the error bands, each group of similar astrophysical conditions retains the overall trends found in the previous individual runs of figure 11. Variation in similar conditions does however blur the exact location of the local minimums. For hot conditions the minimum may be around $N = 100$, 102, and 104 while the position of the minimum may be around $N = 97$, 99 and 101 in the colder scenarios. The observation that the overall trends remain the same, and that there are only shifts in the local minimums to even-N or odd-N nuclei, implies that the mechanisms for peak formation are the same for similar astrophysical conditions. This suggests that future measurements in this region have the potential to uncover trends in the mass surface that might point to characteristics of the r-process site.

3.2. Localized rare earth feature

There is also the possibility that the feature responsible for rare earth peak formation is more localized in proton number. We explore this by setting the falloff parameter to a fixed value of $f = 10$ and allowing the a_Ns and center of the strength in proton number, C, to vary.

The combined results for the more tightly localized mass surfaces predicted for each type of astrophysical conditions are shown in figure 13. For the colder scenarios, the trends are similar those in figure 12, and the C parameter converges to the same value of $Z \sim 60$. The combination of the hot conditions, however, show less of a discernible trend. It is not that the rare earth peak is no longer formed, or that the algorithm does not converge. Rather, we find a large variation in the predicted mass surface trends and different values for C among the three hot evolutions; when the three are combined the individual details of each are washed out and large error bars remain.

These results can be understood from the different freeze-out behaviors of the trajectories. The spread of a broad, persistent mass feature can accommodate a range of path freeze-out positions, but a more localized feature must be tuned carefully to each individual scenario. In particular, the r-process paths at freeze-out for the hot trajectories are close to stability, with the exact locations depending sensitively on the temperature and density at neutron exhaustion. As a result, our algorithm finds three distinct solutions for the three hot trajectories considered here. The discussion of the connection between the predicted mass surface features and freeze-out dynamics continues in the next section.

3.3. Freeze-out dynamics and depth of rare earth dip

As we have seen, the mechanism for rare earth peak formation couples the trends in the masses with the astrophysical conditions. We now discuss this in a more quantitative fashion

Table 2. Information on rare earth peak formation for each trajectory studied in this work, from the reverse-engineering runs that assume a persistent ($f = 40$) feature as described in section 3.1. Definitions of each column are found in the text.

Traj.	Type	ΔA_{LT}	ΔA_{PF}	Δt	$\Delta A_{PF}/\Delta t$	Dip depth (MeV)
1	Hot	0.4	3.8	0.23	16.5	0.68
2	Hot	0.5	3.1	0.18	17.3	0.72
3	Hot	0.6	2.7	0.15	18.0	0.74
4	Cold	1.9	0.9	0.04	22.5	1.13
5	Cold	1.7	1.4	0.06	23.3	0.98
6	Cold	2.0	0.9	0.04	23.1	1.03
7	Very n-rich cold	1.9	1.3	0.05	26.0	1.16
8	Very n-rich cold	2.2	1.4	0.05	28.0	1.32
9	Very n-rich cold	2.1	1.7	0.06	28.3	1.34

by linking the depth of the predicted feature in the mass surface to the late-time *r*-process dynamics.

We define the abundance-weighted shift in atomic mass number during rare earth peak formation due to neutron captures and photodissociations as

$$\Delta A_{PF} = \int_{t(R \sim 1)}^{t\left(\frac{\tau_\beta}{\tau_{n\gamma}} \sim 1\right)} \lambda_{n\gamma} - \lambda_{\gamma n} \, dt, \tag{9}$$

where $\lambda_{n\gamma}$ and $\lambda_{\gamma n}$ are the abundance-weighted average neutron capture and photodissociation rates, respectively, in units of s^{-1}, and the integration is performed from the time at which the neutron-to-seed ratio, R, is unity until the abundance-weighted timescales for neutron capture and β-decay are roughly equal. A definition of abundance-weighted timescales and their inverses, the λ's, can be found in [45]. We define the late-time shift in atomic mass number due to neutron captures as

$$\Delta A_{LT} = \int_{t\left(\frac{\tau_\beta}{\tau_{n\gamma}} \sim 1\right)}^{t(end)} \lambda_{n\gamma} \, dt, \tag{10}$$

where the range of time is between when the abundance-weighted timescales for neutron capture and β-decay are equal and the end of the simulation. The second term in the integrand of equation (9) does not appear in equation (10) since it is negligible for $t > t\left(\frac{\tau_\beta}{\tau_{n\gamma}} \sim 1\right)$. The net neutron capture rate during rare earth peak formation can be approximated by taking the ratio of ΔA_{PF} to the difference in time, Δt, associated with the integration range.

In table 2 we compare the freeze-out quantities defined above to the reverse-engineering results from section 3.1. In that section we found that the results for hot trajectories have a dip in the mass surface centered at higher neutron number than the results for the colder trajectories do. The late-time shift in atomic mass due to neutron captures, ΔA_{LT}, shows a clear difference between the warmer and colder evolutions. The distinct rare earth peak formation mechanisms identified for the hot and cold trajectories by our reverse-engineering studies are attributed to this difference. In hot evolutions there is little late-time bulk transfer of material in A, thus the peak forms in the right spot. In contrast, the greater availability of neutrons late in freeze-out in the colder evolutions favors the peak to form off-center, to the left in atomic mass, with the final placement achieved by late-time neutron captures.

We find that a faster movement of material through the rare earth region during peak formation requires a larger dip in the mass surface, as seen comparing the last two columns of
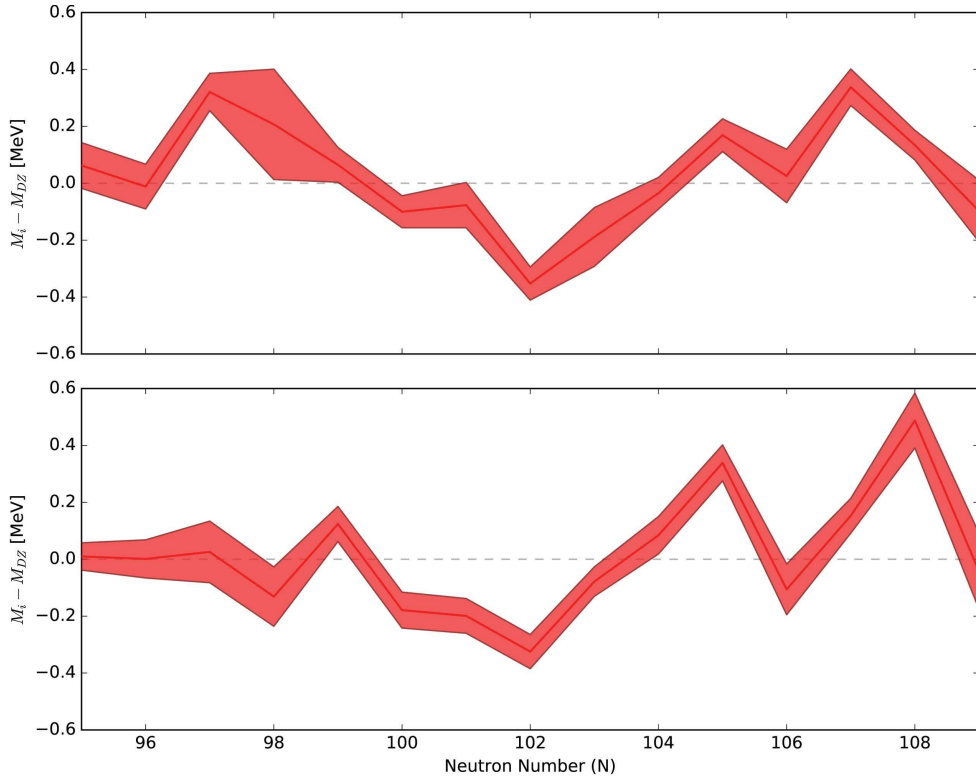
Figure 14. The predicted trends in the mass surface remain relatively unchanged from the use of CoH neutron capture rates (top panel) assuming different neutron capture rates (Nonsmoker—bottom) in a hot, low entropy *r* process (traj. 1).

table 2. This near linear relationship suggests that future mass measurements which find a trend may be able to shed light on how quickly the *r*-process path moves through the region of the *NZ*-plane where the peak is formed.

3.4. Systematic uncertainties

Calculations of the *r* process have many theoretical uncertainties which may impact the application of the reverse engineering framework. We now cover several possibilities and discuss the impact on our conclusions.

Model predictions of neutron capture rates generally range between a factor of 3 in the rare earth region using similar model inputs of LD, γSF and OMP, as shown in figure 3. To test whether this variation in rates has an impact on our results, we implement the results of a second statistical model code, NONSMOKER [53]. The available compilation of NON-SMOKER rates was calculated using FRDM1995 masses. Thus, we first perform the same fitting procedure as in section 2.2 to generate a set of temperature-dependent parameters $a(N, T)$, $b(N, T)$, $c(N, T)$ from the compiled NONSMOKER rates and the FRDM1995 masses. The reverse engineering framework is then used to find the mass surface responsible for rare earth peak formation, using the NONSMOKER capture rate parameters $a(N, T)$, $b(N, T)$, and $c(N, T)$.
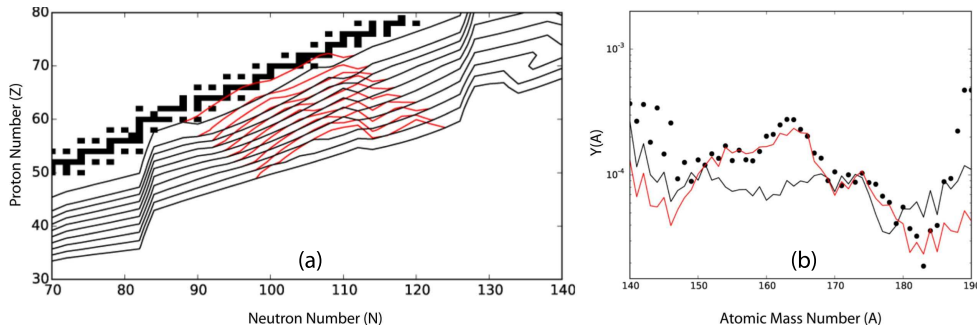
23

Figure 15. One neutron separation energies from DZ (Left panel) and final rare earth peak (right panel) shown in black. The same data is again shown in red when using the algorithm to attempt to reproduce the observed abundances. In this case, the parameter set does not simultaneously match the known masses and can be ruled out.

We compare the mass surface with NONSMOKER rates (bottom panel) to the results of the baseline CoH rates (top panel) in figure 14 for the case of the hot, low entropy r process. We find that both the minimum position of the dip and the overall trend in neutron number of the mass surface remains relatively unchanged with the change of neutron capture rate datasets. This suggests that our conclusions are fairly robust in terms of reasonable variations in neutron capture rates.

It may be argued that still larger systematic uncertainties plague predictions of neutron capture rates in the rare earth region from missing physics in the model inputs. For example, an enhancement of the γSF with missing M1 strength from low energy magnetic radiation or 'LEMAR' was suggested recently by [79, 80]. Preliminary calculations suggested that including the low-lying M1 strength could result in rates larger by a factor of 5–10, which could impact the rare earth region [81], while more recent calculations [82] found a smaller influence on the rates and a minimal impact on the final r-process abundances [82] also found that switching between the Koning OMP and the deformed Kunieda OMP made very little difference (on the order of a factor of 2 or less) in the predictions of neutron capture rates in the rare earth region. The impact of LD calculations on rare earth abundances has yet to be studied and will be the subject of future work.

Modern predictions of rare earth β-decay rates are in fairly good agreement, showing roughly a factor of 2 deviation between model calculations at high Q_β [52, 65, 67]. We explored the impact of this factor of two rate deviation on our reverse-engineering studies in [83]. We reran a selected set of the studies from section 3.1 with rare earth β-decay rates everywhere either increased or decreased by a factor of two. We found that the height of the rare earth peak and the extent of the feature in the mass surface were both changed. If C was held constant and the β-decay rates were increased, the dip in the rare earth mass surface would become larger to compensate for the change. For a slowdown in β-decay rates, the dip in the rare earth mass surface became more shallow. In either case of speeding up or slowing down rare earth β-decay rates, the mechanism for peak production remained the same in both hot and cold environments.

Another possible starting point for our reverse engineering framework is to use the parameters of the DZ mass model as our Monte Carlo parameters. Using feedback only from the rare earth abundances, e.g., only equation (6) is used in the calculation of the likelihood function, we find the mass surface (red lines) shown in the left panel of figure 15. In this case the Monte Carlo parameters successfully produce the rare earth peak (red curve in the right

panel), however, it does so at the expense of the match to measured masses. If we constrain both the measured masses and the rare earth abundances by including both equations (6) and (7) in the likelihood function, we can find no combination of parameters that produces the rare earth peak. This result shows that additional parameters are needed to explain the formation of the rare earth peak using this mass model.

4. Summary

While there are large uncertainties in the inputs to *r*-process nucleosynthesis, the output—the pattern of solar *r*-process residuals—is relatively well known. This opens up the *r* process to treatment as an inverse problem. Here we have developed a Monte Carlo framework to reverse engineer unknown nuclear properties using a quantitative match to the solar isotopic pattern, starting from a range of different astrophysical conditions. Ultimately, we aim to correlate engineered nuclear structure features to characteristics of possible *r*-process environments, such that future experiments can search for these features and thus help to constrain the *r*-process site.

In this work, we have applied our reverse-engineering framework to the neutron-rich rare earth region in an attempt to understand the mass trends responsible for the formation of the rare earth peak. Our procedure starts with DZ masses, which are featureless in the rare earth region and produce flat abundance predictions, and finds solutions with mass modifications to DZ that reproduce the rare earth peak to within the solar isotopic pattern uncertainties. We look for two types of solutions: those that result in a persistent feature in the mass surface that spans a large range in proton number *Z*, and those which produce a feature more localized in *Z*. In both cases, the trends found in the mass surface responsible for rare earth peak production depend on the adopted astrophysical conditions.

When a persistent feature is assumed, we find traditional, hot *r*-process trajectories that go through a long duration $(n, \gamma) \rightleftarrows (\gamma, n)$ equilibrium require trends in masses near $Z = 60$ neodymium isotopes that have local minimums at even-*N* nuclei near $N \sim 100$ and span a change of no more than 0.8 MeV. Colder *r*-process trajectories that have a short duration $(n, \gamma) \rightleftarrows (\gamma, n)$ equilibrium are found to require trends in the mass surface that have local minimums at odd-*N* and span a change of over 1 MeV. We find that the depth of the feature in the masses near $N \sim 100$ is directly related to how far the *r*-process path proceeds towards the neutron dripline and how fast it moves back to stability. In all cases, the trends in the predicted masses are extended in neutron number and are not the abrupt changes that might be expected, e.g., from a subshell closure. Nuclear deformation is a possible source of these smooth trends. When we look for a localized feature, we find solutions that depend more sensitively on the details of the astrophysical conditions. This is most pronounced in the case of hot trajectories where we find a larger deviation between the resultant mass surfaces.

Our results suggest that a wealth of information can be obtained from new measurements in the rare earth region. If a sizable region of enhanced stability is found, its characteristics could point to the nature of the *r*-process site: hot, cold, or very neutron-rich cold. More detailed information about freeze-out conditions could potentially be extracted from the location and depth of a small, localized region of enhanced stability. The absence of any significant feature would disfavor the dynamical method of rare earth peak formation. This would point instead to a rare earth peak composed of fission fragments, which would argue for neutron star mergers as the main *r*-process astrophysical site. It would also be possible to use this method to consider partial fission/partial dynamical solutions for any given prediction of fission rates and daughter distributions.

The past few years has seen a dramatic increase in the quantity and quality of experimental data for neutron-rich nuclei important for the *r* process, e.g., [28, 64, 66, 84–102]. Future measurement campaigns at current and planned experimental facilities such as the FRIB, will offer an unprecedented access to the production of short-lived isotopes [103]. Our study has pinpointed nuclei in the rare earth region which have a substantial impact on the formation of the rare earth peak. A combined theoretical and experimental effort will help to distinguish between astrophysical conditions, thus providing an avenue for moving forward with the solution of the site(s) of the *r* process.

Acknowledgments

References

[1] Turner M 2003 *Connecting Quarks with the Cosmos: Eleven Science Questions for the New Century* (Washington, DC: The National Academies Press)
[2] National Research Council 2013 *Nuclear Physics: Exploring the Heart of Matter* (Washington, DC: The National Academies Press)
[3] Marti K and Zeh H D 1985 History and current understanding of the Suess abundance curve *Meteoritics* **20** 311–20
[4] Arlandini C, Käppeler F, Wisshak K, Gallino R, Lugaro M, Busso M and Straniero O 1999 Neutron capture in low-mass asymptotic giant branch stars: cross sections and abundance signatures *Astrophys. J.* **525** 886–900
[5] Qian Y-Z and Wasserburg G J 2001 A model for abundances in metal-poor stars *Astrophys. J.* **559** 925–41
[6] Travaglio C, Gallino R, Arnone E, Cowan J, Jordan F and Sneden C 2004 Galactic evolution of Sr, Y, And Zr: a multiplicity of nucleosynthetic processes *Astrophys. J.* **601** 864–84
[7] Aoki W, Honda S, Beers T C, Kajino T, Ando H, Norris J E, Ryan S G, Izumiura H, Sadakane K and Takada-Hidai M 2005 spectroscopic studies of very metal-poor stars with the subaru high dispersion spectrograph: III. Light neutron-capture elementsm *Astrophys. J.* **632** 611–37
[8] Montes F *et al* 2007 Nucleosynthesis in the early galaxy *Astrophys. J.* **671** 1685–95
[9] Hansen C J, Montes F and Arcones A 2014 How many nucleosynthesis processes exist at low metallicity? *Astrophys. J.* **797** 123
[10] Wasserburg G J, Busso M and Gallino R 1996 Abundances of actinides and short-lived nonactinides in the interstellar medium: diverse supernova sources for the r-processes *Astrophys. J.* **466** L109
[11] Qian Y-Z and Wasserburg G J 2007 Where, oh where has the r-process gone? *Phys. Rep.* **442** 237–68
[12] Shibagaki S, Kajino T, Mathews G J, Chiba S, Nishimura S and Lorusso G 2016 Relative contributions of the weak, main, and fission-recycling r-process *Astrophys. J.* **816** 79
[13] Cowan J J, Burris D L, Sneden C, McWilliam A and Preston G W 1995 Evidence of heavy element nucleosynthesis early in the history of the galaxy: the ultra-metal-poor star CS 22892-052 *Astrophys. J.* **439** L51–4
[14] Sneden C, Cowan J J and Gallino R 2008 Neutron-capture elements in the early galaxy *Annu. Rev. Astron. Astrophys.* **46** 241–88

[15] Li H-N, Zhao G, Christlieb N, Wang L, Wang W, Zhang Y, Hou Y and Yuan H 2015 Spectroscopic analysis of metal-poor stars from LAMOST: early results *Astrophys. J.* **798** 110

[16] Roederer I U, Lawler J E, Cowan J J, Beers T C, Frebel A, Ivans I I, Schatz H, Sobeck J S and Sneden C 2012 Detection of the second r-process peak element tellurium in metal-poor stars *Astrophys. J.* **747** L8

[17] Roederer I U, Preston G W, Thompson I B, Shectman S A and Sneden C 2014 Neutron-capture nucleosynthesis in the first stars *Astrophys. J.* **784** 158

[18] Burbidge E M, Burbidge G R, Fowler W A and Hoyle F 1957 Synthesis of the elements in stars *Rev. Mod. Phys.* **29** 547–650

[19] Cameron A G W 1957 Nuclear reactions in stars and nucleogenesis *Publ. Astron. Soc. Pac.* **69**

[20] Arnould M, Goriely S and Takahashi K 2007 The r-process of stellar nucleosynthesis: astrophysics and nuclear physics achievements and mysteries *Phys. Rep.* **450** 97–213

[21] Thielemann F-K *et al* 2011 What are the astrophysical sites for the r-process and the production of heavy elements? *Prog. Part. Nucl. Phys.* **66** 346–53

[22] Mumpower M R, Surman R, McLaughlin G C and Aprahamian A 2016 The impact of individual nuclear properties on r-process nucleosynthesis *Prog. Part. Nucl. Phys.* **86** 86–126

[23] Wanajo S 2007 Cold r-process in neutrino-driven winds *Astrophys. J. Lett.* **666** L77

[24] Kortelainen M, McDonnell J, Nazarewicz W, Reinhard P-G, Sarich J, Schunck N, Stoitsov M V and Wild S M 2012 Nuclear energy density optimization: large deformations *Phys. Rev.* C **85** 024304

[25] Erler J, Horowitz C J, Nazarewicz W, Rafalski M and Reinhard P-G 2013 Energy density functional for nuclei and neutron stars *Phys. Rev.* C **87** 044320

[26] Mumpower M, Surman R, Fang D L, Beard M and Aprahamian A 2015 The impact of uncertain nuclear masses near closed shells on the r-process abundance pattern *J. Phys. G: Nucl. Part. Phys.* **42** 034027

[27] Mumpower M R, Surman R, Fang D-L, Beard M, Möller P, Kawano T and Aprahamian A 2015 Impact of individual nuclear masses on r -process abundances *Phys. Rev.* C **92** 035807

[28] Liddick S N *et al* 2016 Experimental neutron capture rate constraint far from stability *Phys. Rev. Lett.* **116** 242502

[29] Martin D, Arcones A, Nazarewicz W and Olsen E 2016 Impact of nuclear mass uncertainties on the r process *Phys. Rev. Lett.* **116** 121101

[30] Käppeler F, Gallino R, Bisterzo S and Aoki W 2011 The s process: nuclear physics, stellar models, and observations *Rev. Mod. Phys.* **83** 157–94

[31] Lodders K, Palme H and Gail H-P 2009 Abundances of the elements in the solar system (arXiv:0901.1149)

[32] Mumpower M R, McLaughlin G C, Surman R and Steiner A W 2016 The link between rare earth peak formation and the astrophysical site of the r process *Astrophys. J* **833** 282

[33] Surman R, Engel J, Bennett J R and Meyer B S 1997 Source of the rare-earth element peak in r-process nucleosynthesis *Phys. Rev. Lett.* **79** 1809–12

[34] Mumpower M R, McLaughlin G C and Surman R 2012 Formation of the rare-earth peak: gaining insight into late-time r-process dynamics *Phys. Rev.* C **85** 045801

[35] Schramm D N and Fowler W A 1971 *Nature* **231** 103

[36] Goriely S, Sida J-L, Lemaître J-F, Panebianco S, Dubray N, Hilaire S, Bauswein A and Janka H-T 2013 New fission fragment distributions and r-process origin of the rare-earth elements *Phys. Rev. Lett.* **111** 242502

[37] Facility for Rare Isotope Beams http://frib.msu.edu/

[38] An International Facility for Antiproton and Ion Research http://fair-center.eu/

[39] Radioactive isotope beam facility at RIKEN http://riken.jp/en/

[40] Metropolis N, Rosenbluth A W, Rosenbluth M N, Teller A H and Teller E 1953 Equation of state calculations by fast computing machines *J. Chem. Phys.* **21** 1087–92

[41] Brooks S P 2003 Bayesian computation: a statistical revolution *Phil. Trans. R. Soc.* A **361** 2681–97

[42] von Toussaint U 2011 Bayesian inference in physics *Rev. Mod. Phys.* **83** 943–99

[43] Arcones A and Martínez-Pinedo G 2011 Dynamical r-process studies within the neutrino-driven wind scenario and its sensitivity to the nuclear physics input *Phys. Rev.* C **83** 045809

[44] Mumpower M R, McLaughlin G C and Surman R 2012 Influence of neutron capture rates in the rare earth region on the r-process abundance pattern *Phys. Rev.* C **86** 035803

[45] Mumpower M R, McLaughlin G C and Surman R 2012 The rare earth peak: an overlooked r-process diagnostic *AAstrophys. J.* **752** 117
[46] Möller P, Nix J R, Myers W D and Swiatecki W J 1995 Nuclear ground-state masses and deformations *At. Data Nucl. Data Tables* **59** 185
[47] Goriely S, Chamel N and Pearson J M 2010 Further explorations of skyrme-hartree-fock-bogoliubov mass formulas: xii. Stiffness and stability of neutron-star matter *Phys. Rev.* C **82** 035804
[48] Liu M, Wang N, Deng Y and Wu X 2011 Further improvements on a global nuclear mass model *Phys. Rev.* C **84** 014333
[49] Koura H, Tachibana T, Uno M and Yamada M 2005 Nuclidic mass formula on a spherical basis with an improved even–odd term *Prog. Theor. Phys.* **113** 305–25
[50] Audi G, Wang M, Wapstra A H, Kondev F G, MacCormick M, Xu X and Pfeiffer B 2012 The Ame2012 atomic mass evaluation *Chin. Phys.* C **36** 2
[51] Duflo J and Zuker A P 1995 Microscopic mass formulas *Phys. Rev.* C **52** 23
[52] Möller P, Pfeiffer B and Kratz K-L 2003 New calculations of gross β-decay properties for astrophysical applications: Speeding-up the classical r process *Phys. Rev.* C **67** 055802
[53] Rauscher T and Thielemann F-K 2000 Astrophysical reaction rates from statistical model calculations *At. Data Nucl. Data Tables* **75** 1–351
[54] Kawano T, Chiba S and Koura H 2006 Phenomenological nuclear level densities using the ktuy05 nuclear mass formula for applications off-stability *J. Nucl. Sci. Technol.* **43** 1–8
[55] Kawano T, Möller P and Wilson W B 2008 Calculation of delayed-neutron energy spectra in a quasiparticle random-phase approximation Hauser-Feshbach model *Phys. Rev.* C **78** 054601
[56] Kawano T, Talou P, Chadwick M B and Watanabe T 2010 Monte carlo simulation for particle and -ray emissions in statistical Hauser-Feshbach model *J. Nucl. Sci. Technol.* **47** 462–9
[57] Kawano T, Capote R, Hilaire S and Huu-Tai P C 2016 Statistical Hauser-Feshbach theory with width-fluctuation correction including direct reaction channels for neutron-induced reactions at low energies *Phys. Rev.* C **94** 014612
[58] Beard M, Uberseder E, Crowter R and Wiescher M 2014 Comparison of statistical model calculations for neutron capture *Phys. Rev.* C **90** 034619
[59] Gilbert A and Cameron A G W 1965 A composite nuclear-level density formula with shell corrections *Can. J. Phys.* **43** 1446
[60] Ignatyuk A V, Smirenkin G N and Tishin A S 1975 Phenomenological description of energy dependence of the level density parameter *Yad. Fiz.* **21** 485–90
[61] Kopecky J and Uhl M 1990 Test of gamma-ray strength functions in nuclear reaction model calculations *Phys. Rev.* C **41** 1941–55
[62] Koning A J and Delaroche J P 2003 Local and global nucleon optical models from 1 keV to 200 MeV *Nucl. Phys.* A **713** 231–310
[63] Goriely S, Hilaire S and Koning A J 2008 Improved predictions of nuclear reaction rates with the TALYS reaction code for astrophysical applications *Astron. Astrophys.* **487** 767–74
[64] Lorusso G *et al* 2015 β-decay half-lives of 110 neutron-rich nuclei across the N = 82 shell gap: implications for the mechanism and universality of the astrophysical r process *Phys. Rev. Lett.* **114** 192501
[65] Shafer T, Engel J, Fröhlich C, McLaughlin G C, Mumpower M and Surman R 2016 Beta decay of deformed r-process nuclei near A = 80 and A = 160, including odd-A and odd–odd nuclei, with the Skyrme finite-amplitude method *Phys. Rev.* C **94** 055802
[66] Wu J *et al* 2016 β-decay half-lives of neutron-rich nuclei around ^{158}Nd, relevant to the formation of the A $\sim$ 165 rare-earth element peak *Eur. Phys. J. Web Conf.* **109** 08003
[67] Marketin T, Huther L and Martínez-Pinedo G 2016 Large-scale evaluation of β-decay rates of r-process nuclei with the inclusion of first-forbidden transitions *Phys. Rev.* C **93** 025805
[68] Möller P, Nix J R and Kratz K-L 1997 Nuclear properties for astrophysical and radioactive-ion beam applications *At. Data Nucl. Data Tables* **66** 131
[69] Mumpower M, Kawano T and Moller P 2016 Neutron-gamma competition for β-delayed neutron emission *Phys. Rev.* C **94** 064317
[70] Eichler M *et al* 2015 The role of fission in neutron star mergers and its impact on the r-process peaks *Astrophys. J.* **808** 30
[71] Möller P, Sierk A J, Ichikawa T, Iwamoto A and Mumpower M 2015 Fission barriers at the end of the chart of the nuclides *Phys. Rev.* C **91** 024310

[72] Hix W R and Thielemann F-K 1999 Computational methods for nucleosynthesis and nuclear energy generation *J. Comput. Appl. Math.* **109** 321–51

[73] Arcones A, Janka H-T and Scheck L 2007 Nucleosynthesis-relevant conditions in neutrino-driven supernova outflows: I. Spherically symmetric hydrodynamic simulations *Astron. Astrophys.* **467** 1227–48

[74] Panov I V and Janka H-T 2009 On the dynamics of proto-neutron star winds and r-process nucleosynthesis *Astron. Astrophys.* **494** 829–44

[75] Goriely S, Bauswein A and Janka H-T 2011 r-process nucleosynthesis in dynamically ejected matter of neutron star mergers *Astrophys. J.* **738** L32

[76] Just O, Bauswein A, Pulpillo R A, Goriely S and Janka H-T 2015 Comprehensive nucleosynthesis analysis for ejecta of compact binary mergers *Mon. Not. R. Astron. Soc.* **448** 541–67

[77] Martínez-Pinedo G, Fischer T and Huther L 2014 Supernova neutrinos and nucleosynthesis *J. Phys. G: Nucl. Phys.* **41** 044008

[78] McLaughlin G C, Fetter J M, Balantekin A B and Fuller G M 1999 Active-sterile neutrino transformation solution for r-process nucleosynthesis *Phys. Rev.* C **59** 2873–87

[79] Schwengner R, Frauendorf S and Larsen A C 2013 Low-energy enhancement of magnetic dipole radiation *Phys. Rev. Lett.* **111** 232504

[80] Frauendorf S, Schwengner R and Wimmer K 2014 Low-energy magnetic radiation: deviations from GOE *Am. Inst. Phys. Conf. Ser.* **1619** 81–8

[81] Frauendorf S, Beard M, Mumpower M, Schwengner R and Wimmer K 2015 Low-energy magnetic radiation *Eur. Phys. J. Web Conf.* **93** 04002

[82] Kawano T, Ullmann J L, Mumpower M R and Krticka M 2016 Estimation of m1 scissor mode strength for deformed nuclei in the medium to heavy mass region by statistical hauser-feshbach model calculations in the fast energy range *Phys. Rev. C* (submitted)

[83] Mumpower M R, McLaughlin G C, Surman R and Steiner A W 2016 The rare earth peak and the astrophysical location of the *r* process

[84] Hakala J *et al* 2012 Precision mass measurements beyond Sn132: anomalous behavior of odd–even staggering of binding energies *Phys. Rev. Lett.* **109** 032501

[85] Madurga M *et al* 2012 New half-lives of r-process Zn and Ga isotopes measured with electromagnetic separation *Phys. Rev. Lett.* **109** 112501

[86] Van Schelt J *et al* 2013 First results from the CARIBU facility: mass measurements on the r-process path *Phys. Rev. Lett.* **111** 061102

[87] Kurtukian-Nieto T *et al* 2014 Beta-decay half-lives of new neutron-rich isotopes of Re, Os and Ir approaching the r-process path near N = 126 *Eur. Phys. J.* A **50** 135

[88] Caballero-Folch R *et al* 2014 β-decay and β-delayed neutron emission measurements at GSI-FRS beyond N = 126, for r-process nucleosynthesis *Nucl. Data Sheets* **120** 81–3

[89] Spyrou A *et al* 2014 Novel technique for constraining r -process (n, γ) reaction rates *Phys. Rev. Lett.* **113** 232502

[90] Sun B H, Litvinov Y A, Tanihata I and Zhang Y H 2015 Toward precision mass measurements of neutron-rich nuclei relevant to r-process nucleosynthesis *Front. Phys.* **10** 503

[91] Atanasov D *et al* 2015 Precision mass measurements of ^{Cd}-131$_{129}$ and their impact on stellar nucleosynthesis via the rapid neutron capture process *Phys. Rev. Lett.* **115** 232501

[92] Klawitter R *et al* 2016 Mass measurements of neutron-rich Rb and Sr isotopes *Phys. Rev.* C **93** 045807

[93] Lascar D *et al* 2016 Improvements to TITAN's mass measurement and decay spectroscopy capabilities *Nucl. Inst. Meth. Phys. Res.* B **376** 292–7

[94] Cizewski J A and Nunes F M 2015 Theoretical and experimental perspectives of nuclear reaction studies with radioactive ion beams *Acta Phys. Pol.* B **46** 521

[95] Mazzocchi C *et al* 2015 β-decay properties of the very neutron-rich isotopes ^{86}Ge and ^{86}As *Phys. Rev.* C **92** 054317

[96] Jones K L *et al* 2015 Recent direct reaction experimental studies with radioactive tin beams *Acta Phys. Pol.* B **46** 537

[97] Dunlop R *et al* 2016 Half-lives of neutron-rich ^{Cd}-130$_{128}$ *Phys. Rev.* C **93** 062801

[98] Alshudifat M F *et al* 2016 Reexamining gamow-teller decays near ^{78}Ni *Phys. Rev.* C **93** 044325

[99] Domingo-Pardo C *et al* 2016 Approaching the precursor nuclei of the third r-process peak with RIBs *J. Phys.: Conf. Ser.* **665** 012045

[100] Miernik K *et al* 2016 β-decay study of ^{94}Kr *Phys. Rev.* C **94** 024305

[101] Caballero-Folch R *et al* 2016 First measurement of several β-delayed neutron emitting isotopes beyond N = 126 *Phys. Rev. Lett.* **117** 012501

[102] Hirsh T Y *et al* 2016 First operation and mass separation with the CARIBU MR-TOF *Nucl. Instrum. Methods Phys. Res.* B **376** 229–32

[103] Horowitz C *et al* 2016 *r*-process nucleosynthesis: connecting rare-isotope beam facilities with the cosmos (submitted)